PHYSICAL REVIEW A **96**, 013405 (2017)

Kinematical vortices in double photoionization of helium by attosecond pulses

J. M. Ngoko Djiokap,[1] A. V. Meremianin,[2] N. L. Manakov,[2] S. X. Hu,[3] L. B. Madsen,[4] and Anthony F. Starace[1]
[1]*Department of Physics and Astronomy, University of Nebraska, Lincoln, Nebraska 68588-0299, USA*
[2]*Department of Physics, Voronezh State University, Voronezh 394006, Russia*
[3]*Laboratory for Laser Energetics, University of Rochester, Rochester, New York 14623, USA*
[4]*Department of Physics and Astronomy, Aarhus University, DK-8000 Aarhus C, Denmark*
(Received 1 May 2017; published 7 July 2017)

Two-armed helical vortex structures are predicted in the two-electron momentum distributions produced in double photoionization (DPI) of the He atom by a pair of time-delayed elliptically polarized attosecond pulses with opposite helicities. These predictions are based upon both a first-order perturbation theory analysis and numerical solutions of the two-electron, time-dependent Schrödinger equation in six spatial dimensions. The helical vortex structures originate from Ramsey interference of a pair of ionized two-electron wave packets, each having a total angular momentum of unity, and appear in the sixfold differential DPI probability distribution for any energy partitioning between the two electrons. The vortex structures are exquisitely sensitive to the time delay between the two pulses, their relative phase, their ellipticity, and their handedness; moreover, they occur in a variety of electron detection geometries. However, the vortex structures only occur when the angular separation $\beta = \cos^{-1}(\hat{\mathbf{p}}_1 \cdot \hat{\mathbf{p}}_2)$ between the electron momenta $\mathbf{p}_1$ and $\mathbf{p}_2$ is held fixed. The vortex structures can also be observed in the fourfold differential DPI probability distribution obtained by averaging the sixfold differential probability over the emission angles of one electron. Such kinematical vortices are a general phenomenon that may occur in any ionization process, initiated by two time-delayed short pulses with opposite ellipticities, for particular detection geometries.

DOI: 10.1103/PhysRevA.96.013405

I. INTRODUCTION

The quantum dynamics of correlated two-electron atomic systems driven by short-wavelength ultrashort laser pulses is one of the most fundamental and intriguing problems in strong-field and attosecond physics. Double photoionization (DPI) of the helium atom by means of linearly polarized synchrotron light sources at vacuum ultraviolet (vuv) and x-ray wavelengths has long been the benchmark for our understanding of correlation effects in the fundamental three-body Coulomb problem [1–7], as it involves absorption of only a single photon. Recent advances in optical technologies have led to the experimental realization of linearly polarized, few-cycle, extreme ultraviolet (xuv) attosecond pulse trains [8] and isolated pulses [9–12] having tunable and stable carrier-envelope phases (CEPs) [10]. These tools have made possible the laser-atom interaction regime in which the pulse wave form, governed by the CEP, matters. Moreover, the pulse durations are comparable to the characteristic time scale associated with electronic motion and electron correlations [13,14].

Despite these advances for the case of linearly polarized attosecond pulses, elliptically polarized attosecond pulses are not yet a reality. However, there is great interest in developing efficient schemes for production of short, coherent xuv pulses with tunable polarizations [15–35]. This interest is motivated by the numerous applications of chiral-sensitive (dichroic) light-matter interactions, such as in photoionization circular dichroism investigations of chiral molecules [36–38], in x-ray magnetic circular dichroism investigations of magnetic materials [39–42], and in nonlinear elliptic dichroism investigations of double-photoionization processes [43].

Recently, we have developed *ab initio* analytical and numerical tools for treating the He atom exposed to two time-delayed ultrashort circularly polarized pulses [44,45]. Intriguing electron phenomena were predicted in photoionized electron momentum distributions, including *two-start* spiral electron vortices in single-electron photoionization by a pair of oppositely circularly polarized attosecond xuv pulses [44] and *multistart* spiral electron vortices in single-electron multiphoton ionization by two circularly polarized uv pulses [45]. These matter wave spiral patterns require the broad bandwidth characteristic of ultrashort pulses and stem from an unusual kind of Ramsey interference of the single-electron wave packets produced by each of the time-delayed, oppositely circularly polarized pulses. Moreover, the *even-start* electron matter-wave vortices from single ionization [44,45] were found to have a counterpart in optics [46], providing thus a dramatic example of wave-particle duality. Our predictions stem from kinematic factors and are thus applicable to single-ionization processes for any target system, as demonstrated recently by Yuan *et al.* [47] for *odd-start* electron vortices in two-color single ionization of the H_2^+ molecule. Very recently, our predicted spiral electron vortices [44,45] were experimentally observed in multiphoton single ionization of potassium atoms by a pair of time-delayed oppositely circularly polarized fs pulses [48]. For two-color, circularly polarized pulses having *zero time delay*, our predictions [45] are consistent with results for two-color single ionization of Ar [49] and H [50] atoms. All of these predicted and observed results concern only single-electron ionization processes. The possibility for observing such vortex patterns in the momentum distributions for two-electron ionization processes has not yet been considered.

In this paper we predict the occurrence of *two-start* Fermat spiral vortices in the two-electron momentum distribution [i.e., the sixfold differential probability (SDP)] for DPI of the He atom by two time-delayed attosecond pulses with opposite ellipticities. We show that these spiral vortex structures in the two-electron momentum distributions occur for any energy partitioning between the electrons and may be observed in both the in-plane and out-of-plane detection geometries defined in Fig. 1. However, the spiral vortex patterns only occur when the angular separation between the two electron momenta, $\beta = \cos^{-1}(\hat{\mathbf{p}}_1 \cdot \hat{\mathbf{p}}_2)$, is held fixed while detecting one of the electron momenta $\mathbf{p}_1$, $\mathbf{p}_2$, $\mathbf{P}_+$, or $\mathbf{P}_-$, where the Jacobi momenta, $\mathbf{P}_\pm$, define respectively the center-of-mass momentum ($\mathbf{P}_+ = \mathbf{p}_1 + \mathbf{p}_2$) and the relative momentum [$\mathbf{P}_- = (\mathbf{p}_1 - \mathbf{p}_2)/2$] of the ionized electron pair [4,51,52]. Such β-fixed detection geometries (which have been termed configurations in which electron-electron correlation is "frozen" [53]) are illustrated in the general case in Fig. 1(a). The specific cases treated in this paper are the in-plane back-to-back (BTB) detection geometry [see Fig. 1(b)], the out-of-plane orthogonal detection geometry [see Fig. 1(c)], and some other out-of-plane geometries [see Fig. 1(a)]. For these β-fixed detection geometries, we show that by varying the ellipticities of the two time-delayed attosecond pulses, the corresponding two-electron momentum distributions exhibit circularly symmetric patterns (for two corotating circularly polarized pulses), dipolar patterns (for two linearly polarized pulses), and two-arm spiral vortex patterns *distorted or not* (for two counterrotating *elliptically or circularly* polarized pulses). Moreover, the sensitivity of the two-electron momentum distributions to the pulse CEPs is also exhibited. Finally, for any energy-sharing configuration, our numerical two-electron time-dependent Schrödinger equation (TDSE) results and analytic perturbation theory (PT) analyses predict a time-delay periodicity for the ionized electron angular distributions that depends upon the pulse-pair ellipticities.

This paper is organized as follows. In Sec. II, we describe our numerical methods for solving the two-electron TDSE in six spatial dimensions for the He atom interacting with a pair of time-delayed elliptically polarized pulses. In Sec. III, we parametrize the first-order PT DPI amplitude in alternative electron momentum bases. In Sec. IV, analytic results for the SDP for DPI by two identically polarized pulses are presented together with illustrative TDSE numerical results for the detection geometries in Figs. 1(b) and 1(c). In Sec. V, analytic results for the SDP for DPI by two counterrotating pulses are presented together with illustrative TDSE numerical results for the β-fixed detection geometries in Fig. 1 that demonstrate spiral vortex patterns in the two-electron momentum distributions. In Sec. VI, we analyze the time-delay periodicity and control of two-electron angular distributions. In Sec. VII, we summarize our results and present our conclusions. Finally, in Appendix A we discuss the convergence of our numerical results for two-electron angular distributions, and in Appendix B, we derive the parametrization of the SDP averaged over the emission angles of one electron [i.e., the fourfold differential probability (FDP)] and demonstrate the occurrence of spiral vortex structures in the FDP. We employ atomic units ($e = m_e = \hbar = 1$) unless specified otherwise.

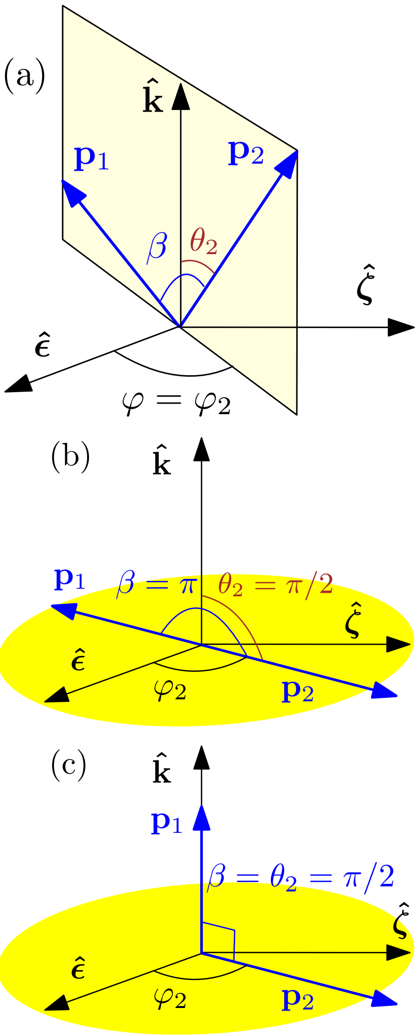

FIG. 1. Detection geometries for observing spiral vortex patterns in the two-electron momentum distribution [i.e., the sixfold differential probability (SDP)] resulting from double photoionization (DPI) of He. In order for spiral vortex patterns to occur in DPI using two oppositely circularly polarized attosecond pulses, the SDP $\mathcal{W}_{\xi,-\xi}$ must be measured for fixed $\beta = \cos^{-1}(\hat{\mathbf{p}}_1 \cdot \hat{\mathbf{p}}_2)$ as a function of φ and one of the electron momenta p_1, p_2, P_+, or P_- (see text for discussion). Panels (a), (b), and (c) illustrate three examples of such β-fixed detection geometries. (a) General detection geometry, in which $\hat{\boldsymbol{\epsilon}}$ and $\hat{\boldsymbol{\zeta}}$ are the major and minor axes of the polarization ellipse of each of the two pulses, both of which are propagating along the $\hat{\boldsymbol{k}}$ axis. (b) Back-to-back (BTB) detection geometry in which the two photoelectrons are emitted in opposite directions (i.e., $\beta = \pi$) in the polarization plane ($\hat{\boldsymbol{\epsilon}}$,$\hat{\boldsymbol{\zeta}}$). (c) An out-of-plane detection geometry in which one electron is detected along $\hat{\boldsymbol{k}}$, while the other is detected in the polarization plane; this geometry defines an orthogonal geometry in which $\beta = \pi/2$. For later use, we define an *in-plane detection geometry* as one in which the electron momenta $\mathbf{p}_1 \equiv (p_1,\theta_1,\varphi_1)$ and $\mathbf{p}_2 \equiv (p_2,\theta_2,\varphi_2)$ are detected in the polarization plane [see, e.g., (b)], and an *out-of-plane detection geometry* as one in which at least one of the electron momenta is detected out of the polarization plane [see, e.g., (a) and (c)]. In the limit of linear polarization, the polarization is along $\hat{\boldsymbol{\epsilon}}$.

II. NUMERICAL METHODS

Our numerical results are based on the *ab initio* solution of the two-electron TDSE in six spatial dimensions for the He atom interacting with a pair of time-delayed, elliptically polarized pulses. Details of our numerical methods can be found elsewhere [43–45]. In brief, we employ a time-dependent close-coupling expansion [54,55] of the wave packet $\Psi(\mathbf{r}_1,\mathbf{r}_2;t)$ onto the orthonormal basis functions of bipolar-spherical harmonics $\Lambda_{l_1,l_2}^{LM}(\hat{\mathbf{r}}_1,\hat{\mathbf{r}}_2)$, where L is the total angular momentum of the two-electron system, M is its azimuthal quantum number, and l_1,l_2 are the individual electron orbital angular momenta. Using the length gauge in the dipole approximation, the two-electron TDSE in six spatial dimensions is solved using a finite-element discrete-variable representation (FE-DVR) [56] combined with the real-space-product algorithm (a split-operator method) [57–60] together with Wigner rotation transformations at each time step from the laboratory frame to the frame of the instantaneous electric field [61,62]. At the end of the two pulses, i.e., at $t = T_f$, we freely propagate the two-electron wave packet $\Psi(\mathbf{r}_1,\mathbf{r}_2;t)$ for a time T_p before extracting the SDP [63] for DPI of He by projecting the two-electron continuum part, $\Psi_C(\mathbf{r}_1,\mathbf{r}_2;T_f+T_p)$, of the wave packet $\Psi(\mathbf{r}_1,\mathbf{r}_2;T_f+T_p)$ onto the double-continuum final state, which is approximated by a product of two Coulomb waves $\Psi^{(-)}_{\mathbf{p}_1,\mathbf{p}_2}(\mathbf{r}_1,\mathbf{r}_2)$ with charge $Z = 2$. The SDP, $\mathcal{W}(\mathbf{p}_1,\mathbf{p}_2)$, for producing two continuum electrons with momenta $\mathbf{p}_1$ and $\mathbf{p}_2$ is thus

$$\mathcal{W}(\mathbf{p}_1,\mathbf{p}_2) = |\langle\Psi^{(-)}_{\mathbf{p}_1,\mathbf{p}_2}(\mathbf{r}_1,\mathbf{r}_2)|\Psi_C(\mathbf{r}_1,\mathbf{r}_2,T_f+T_p)\rangle|^2. \tag{1}$$

We include four total angular momenta, $L = 0$–3, and all allowed combinations of individual electron orbital angular momenta $l_1,l_2 = 0$–5 and azimuthal quantum numbers $|M| \leqslant L$, $|m_1| \leqslant l_1$, and $|m_2| \leqslant l_2$.

To discretize the radii r_1 and r_2, we adopt a FE-DVR [56] in which 60 finite elements equally spaced by 2 a.u. are used. An eight-point Gauss-Legendre-Lobatto basis is used within each finite element, which yields a total of 421 DVR functions in each radial coordinate up to 120 a.u. The connection between neighboring elements is made using a bridge function that guarantees continuity across the element boundaries.

After solving the TDSE, the doubly ionized wave packet $\Psi_C(\mathbf{r}_1,\mathbf{r}_2;T_f+T_p)$ is obtained by subtracting from the total wave packet $\Psi(\mathbf{r}_1,\mathbf{r}_2;T_f+T_p)$ both the bound state and the single continuum parts. To achieve this, we implement the procedure of Ref. [63] in which the total wave packet is set equal to zero for radial distances $r_1 < R_0$ or $r_2 < R_0$, where R_0 defines the outer radial boundary of bound and single continuum states. For our pulse parameters, varying R_0 between 5 and 15 a.u. does not change our predictions for the SDP. All results presented here have been obtained for $R_0 = 10$ a.u.

For typical pulse parameters used throughout this paper, convergence tests for the DPI angular distributions produced by pairs of time-delayed elliptically polarized pulses are presented and discussed in Appendix A. The tests find numerically the projection times T_p (after the end of the two pulses) at which the numerically calculated angular distributions converge. Specifically, we use a projection time $T_p = 30$ a.u. ($T_p = 45$ a.u.) for the unequal (equal) energy-sharing cases reported below; see Fig. 9 and discussion in Appendix A.

III. FIRST-ORDER PERTURBATION THEORY TRANSITION AMPLITUDE

Consider the helium atom (with single- and double-ionization threshold energies, $E_b = 24.59$ eV and $E_g = 79.01$ eV) interacting with a pair of attosecond pulses delayed in time by τ, with each pulse having the same carrier frequency $\omega > E_g$. If each pulse has a peak intensity I below 10^{14} W/cm^2, then double ionization occurs primarily by single-photon absorption. In this work, $\omega = 90$ eV and $I = 5\times10^{13}$ W/cm^2, so that the ponderomotive energy $I/4\omega^2$ of 0.85 meV is very small; i.e., we are in the perturbative multiphoton regime where PT applies. Hence, throughout this paper we adopt PT to guide and analyze our numerical TDSE results. The excellent agreement between our numerical TDSE results and our first-order PT results presented in Sec. VI confirms our assumption that DPI occurs by single-photon absorption. This assumption implies also that (i) nonlinear effects from higher-order (beyond first-order) processes produced by a single pulse are negligible, and that (ii) the rotating-wave approximation (RWA) is valid; i.e., photon emission processes are extremely small (and can thus be neglected in our PT analyses). Therefore, our study for DPI can be focused on the excess energy range $E = \omega \pm \Delta\omega - E_g$ (i.e., for $0 \leqslant E \leqslant 32.6$ eV) above the threshold that can be shared by the two electrons, where $\Delta\omega \simeq 1.44\omega/N$ [13] is the bandwidth for a pulse having a cosine-squared temporal envelope, with N being the number of optical cycles—in our case $N = 6$ and $\Delta\omega \simeq 21.6$ eV. As in Refs. [44,45] and as discussed below, the broad bandwidth characteristic of isolated attosecond pulses is essential to observe well-defined vortex patterns or, equivalently, clearly defined Ramsey interference patterns, which require that $2\pi/\tau < \Delta\omega$.

In PT, the SDP for DPI of He by a pair of pulses is

$$\mathcal{W}(\mathbf{p}_1,\mathbf{p}_2) \equiv \frac{d^6W}{d\mathbf{p}_1 d\mathbf{p}_2} = |A(\mathbf{p}_1,\mathbf{p}_2)|^2, \tag{2}$$

where $A(\mathbf{p}_1,\mathbf{p}_2)$ is the PT transition amplitude for producing two electrons in the continuum with momenta $\mathbf{p}_1$ and $\mathbf{p}_2$. In the dipole interaction of the He atom with the electric field $\mathbf{F}(t)$ under the PT assumption (i), $A(\mathbf{p}_1,\mathbf{p}_2)$ reduces to its first-order result:

$$A_1 = -i\int_{-\infty}^{+\infty} e^{iE_f t}\langle\Psi^{(-)}_{\mathbf{p}_1,\mathbf{p}_2}|\mathbf{F}(t)\cdot\mathbf{d}|{}^1S^e\rangle e^{-iE_i t}\,dt, \tag{3}$$

where $\mathbf{d} = \mathbf{r}_1 + \mathbf{r}_2$ is the electric dipole moment operator of the two electrons, $\Psi^{(-)}_{\mathbf{p}_1,\mathbf{p}_2}$ is the two-electron continuum wave function with energy $E = E_1 + E_2$, $E_i = -E_g$ is the initial-state energy, and $E_f = E + E_{\mathrm{He}^{2+}}$ is the final-state energy. For a bare ion energy $E_{\mathrm{He}^{2+}} = 0$, the energy of the He ground state, $|{}^1S^e\rangle$, is $-E_g = -2.9037$ a.u. In Eq. (3), we consider an electric field $\mathbf{F}(t)$ of a pair of time-delayed arbitrarily polarized pulses having the same carrier frequency ω and intensity $I = F_0^2$, where F_0 is the electric field strength. The general form of such an electric field $\mathbf{F}(t)$ is

$$\begin{aligned}\boldsymbol{F}(t) = \boldsymbol{F}_1(t) + \boldsymbol{F}_2(t-\tau) \equiv F_0^{(1)}(t)\,\mathrm{Re}[\mathbf{e}_1 e^{-i(\omega t+\phi_1)}]\\ + F_0^{(2)}(t-\tau)\,\mathrm{Re}[\mathbf{e}_2 e^{-i[\omega(t-\tau)+\phi_2]}],\end{aligned} \tag{4}$$

where for the jth pulse ($j=1,2$), $\mathbf{e}_j$ is its polarization, ϕ_j is its CEP, $F_0^{(j)}(t)/F_0=\cos^2(\pi t/T_j)$ is its temporal envelope, and $T_j=N_j(2\pi/\omega)$ is its duration, with N_j being the number of cycles in the pulse. It is useful to define the polarization vector of the jth pulse as

$$\mathbf{e}_j \equiv (\hat{\boldsymbol{\epsilon}} + i\eta_j\hat{\boldsymbol{\zeta}})\Big/\sqrt{1+\eta_j^2}, \tag{5}$$

where $\hat{\boldsymbol{\epsilon}}$ and $\hat{\boldsymbol{\zeta}} \equiv \hat{\mathbf{k}} \times \hat{\boldsymbol{\epsilon}}$ are respectively the major and minor axes of the polarization ellipse, and $\hat{\boldsymbol{k}} \parallel \hat{\mathbf{z}}$ is the pulse propagation direction. Denoting the ellipticity of the jth pulse by η_j ($-1 \leqslant \eta_j \leqslant +1$), its degrees of linear and circular polarization are $\ell_j \equiv (\mathbf{e}_j \cdot \mathbf{e}_j) = (1-\eta_j^2)/(1+\eta_j^2)$ and $\xi_j \equiv \mathrm{Im}\,[\mathbf{e}_j^* \times \mathbf{e}_j]_z = 2\eta_j/(1+\eta_j^2)$, respectively.

Each pulse $\boldsymbol{F}_j(t)$ in Eq. (4) has components $\boldsymbol{F}_j^{\pm}(t)$ for photon absorption ($+$) and photon emission ($-$), i.e.,

$$\begin{aligned}\boldsymbol{F}_j(t) =& \boldsymbol{F}_j^{+}(t) + \boldsymbol{F}_j^{-}(t) \equiv [F_0^{(j)}(t)/2][\mathbf{e}_j e^{-i(\omega t+\phi_j)}] \\ &+ [F_0^{(j)}(t)/2][\mathbf{e}_j^* e^{+i(\omega t+\phi_j)}].\end{aligned} \tag{6}$$

Under the above RWA approximation (ii), the photon emission contributions from $\boldsymbol{F}^{-}(t)=[\boldsymbol{F}^{+}(t)]^*$ are extremely small and are thus neglected in the PT analysis. Hence, only the photon absorption parts of the electric field (4) are retained for our pair of pulses:

$$\begin{aligned}\boldsymbol{F}^{+}(t) \equiv& \boldsymbol{F}_1^{+}(t) + \boldsymbol{F}_2^{+}(t-\tau) = [F_0^{(1)}(t)/2]e^{-i(\omega t+\phi_1)}\mathbf{e}_1 \\ &+ [F_0^{(2)}(t-\tau)/2]e^{-i[\omega(t-\tau)+\phi_2]}\mathbf{e}_2.\end{aligned} \tag{7}$$

The first-order PT transition amplitude (3) for DPI by single-photon absorption from the initial ${}^1S^e$ ground state with energy E_i to the continuum ${}^1P^o$ state of the electron pair with energy $E_f=E$ thus has the form

$$A_1 = -i(F_0/2)e^{-i\phi_1}\langle\Psi^{(-)}_{\mathbf{p}_1,\mathbf{p}_2}|\mathbf{e}'\cdot\mathbf{d}|\,{}^1S^e\rangle. \tag{8}$$

In Eq. (8), the effective polarization vector $\mathbf{e}'$ is

$$\mathbf{e}' = J_1\mathbf{e}_1 + J_2 e^{i\Phi}\mathbf{e}_2, \tag{9}$$

where J_j ($j=1,2$) are given by the auxiliary expression

$$J_j = \int_{-\infty}^{+\infty}\cos^2(\pi t/T_j)\,e^{i\epsilon t}\,dt = -\frac{\sin(\pi N_j\epsilon/\omega)}{\epsilon[(N_j\epsilon/\omega)^2-1]}, \tag{10}$$

where $\epsilon = E_f - E_i - \omega$. The relative phase Φ in Eq. (9),

$$\Phi = (E_f - E_i)\tau + \phi_{12}, \tag{11}$$

is composed of two contributions: $(E_f-E_i)\tau$, the difference in the phase accumulation during the temporal evolution of the two electronic wave packets for a time delay τ, and $\phi_{12} \equiv \phi_1 - \phi_2$, the difference between the CEPs of the pair of pulses. For DPI of He we have

$$\Phi = [\big(p_1^2+p_2^2\big)/2 + E_g]\tau + \phi_{12}. \tag{12}$$

Note that Φ in Eq. (11) has the same form as in Ref. [44] for single-photoionization processes.

Although the matrix element (8) has the same form as in the case of a conventional DPI process [6], the effective double-pulse polarization vector $\mathbf{e}'$ in (8) [which is not normalized, $(\mathbf{e}'\cdot\mathbf{e}'^*) \neq 1$] enables one to "turn off" the ionization by tuning the double-pulse parameters. Specifically, for DPI by two identical pulses delayed in time by τ, we have $\mathbf{e} \equiv \mathbf{e}_1 = \mathbf{e}_2$ and $J \equiv J_1 = J_2$. Thus, $\mathbf{e}' = J[1+\exp(i\Phi)]\,\mathbf{e} = 0$ for $\exp(i\Phi)=-1$, and hence the first-order amplitude A_1 (8) vanishes. According to Eq. (11), values of $\Phi = \pi(2n+1)$, $n=0,1,2,\ldots,$ can be set by tuning the relative CEP and/or the time delay τ.

In the following subsections, we parametrize our general expression (8) for the DPI transition amplitude in three different momentum bases, which are convenient for analyzing our results in different cases of energy-sharing configurations, detection geometries, and polarization states of the two pulses.

A. Basis of reduced two-electron momenta $\mathbf{p}_{\pm}$

We introduce the reduced two-electron momenta $\mathbf{p}_{\pm}$,

$$\mathbf{p}_{\pm} = (\hat{\mathbf{p}}_1 \pm \hat{\mathbf{p}}_2)/2, \tag{13}$$

in terms of the unit momentum vectors $\hat{\mathbf{p}}_{1,2}$. They obey the relations $(\mathbf{p}_+\cdot\mathbf{p}_-)=0$, $p_+=\cos(\beta/2)$, and $p_-=\sin(\beta/2)$, where $\cos\beta = \hat{\mathbf{p}}_1\cdot\hat{\mathbf{p}}_2$. In terms of $\mathbf{e}'$ and $\mathbf{p}_{\pm}$, the amplitude (8) takes the form [52]

$$A_1 = -ie^{-i\phi_1}[f_+(\mathbf{e}'\cdot\mathbf{p}_+) + f_-(\mathbf{e}'\cdot\mathbf{p}_-)], \tag{14}$$

where the parameters $f_{\pm}$ are defined by

$$f_{\pm} = (F_0/2)\langle\Psi^{(-)}_{\mathbf{p}_1,\mathbf{p}_2}|\mathbf{p}_{\pm}\cdot\mathbf{d}|\,{}^1S^e\rangle. \tag{15}$$

For the BTB geometry $\mathbf{p}_+=0$, so that the term involving f_+ is absent from the amplitude A_1 in Eq. (14).

The parameters $f_{\pm}$ are the same as in a conventional DPI process [6]. In particular, they are independent of the pulse polarization, time delay, and CEPs, i.e., $f_{\pm}=f_{\pm}(p_1,p_2,\cos\beta)$. Expressions for $f_{\pm}$ in terms of radial matrix elements of the dipole operator can be found in Ref. [64]. These are not used in the present treatment as the probability has been calculated by means of the direct numerical solution of the TDSE, as in Ref. [45].

From the Pauli exclusion principle, the parameters $f_{\pm}$ obey the following symmetry relations:

$$f_+(p_2,p_1,\cos\beta) = (-1)^S f_+(p_1,p_2,\cos\beta), \tag{16}$$

$$f_-(p_2,p_1,\cos\beta) = (-1)^{S+1} f_-(p_1,p_2,\cos\beta), \tag{17}$$

where $S=0$ ($S=1$) for a singlet (triplet) initial state. For an initial singlet state ($S=0$) and equal energy sharing between electrons ($p_1=p_2=p$), it follows from Eq. (17) that $f_-(p,p,\cos\beta)=0$.

B. Basis of conventional momenta $\mathbf{p}_{1,2}$

From Eqs. (13)–(15) one can parametrize the amplitude in terms of the conventional vectors $\mathbf{p}_{1,2}$ as

$$A_1 = -ie^{-i\phi_1}[f_1(\mathbf{e}'\cdot\hat{\mathbf{p}}_1) + f_2(\mathbf{e}'\cdot\hat{\mathbf{p}}_2)], \tag{18}$$

where the parameters $f_{1,2}$ are defined by

$$f_1 = (f_+ + f_-)/2, \quad f_2 = (f_+ - f_-)/2. \tag{19}$$

Under particle exchange, the parameters $f_{1,2}$ satisfy

$$f_1(p_2,p_1,\cos\beta) = (-1)^S f_2(p_1,p_2,\cos\beta). \tag{20}$$

C. Basis of Jacobi momenta $\mathbf{P}_\pm$

The Jacobi momenta, $\mathbf{P}_\pm$, defined by

$$\mathbf{P}_+ = \mathbf{p}_1 + \mathbf{p}_2,\ \mathbf{P}_- = (\mathbf{p}_1 - \mathbf{p}_2)/2, \tag{21}$$

are useful for describing collective two-electron motions [4,51,52]. The parametrization of A_1 in terms of these momenta is

$$A_1 = -ie^{-i\phi_1}[f_+^J(\mathbf{e}'\cdot\hat{\mathbf{P}}_+) + f_-^J(\mathbf{e}'\cdot\hat{\mathbf{P}}_-)]. \tag{22}$$

Here the dynamical parameters $f_\pm^J$, defined by

$$f_+^J = \frac{P_+}{2}\left(\frac{f_1}{p_1} + \frac{f_2}{p_2}\right),\quad f_-^J = P_-\left(\frac{f_1}{p_1} - \frac{f_2}{p_2}\right), \tag{23}$$

depend only on the angular separation, $\kappa = \hat{\mathbf{P}}_+\cdot\hat{\mathbf{P}}_-$, between the momenta and their magnitudes $P_+ = \sqrt{2E}[1 + 2\sqrt{\varepsilon(1-\varepsilon)}\cos\beta]^{1/2}$ and $P_- = \sqrt{2E}[1 - 2\sqrt{\varepsilon(1-\varepsilon)}\cos\beta]^{1/2}/2$, where $\varepsilon = E_1/E$ defines the degree of energy sharing between the two electrons. Under electron exchange, $\mathbf{p}_1 \leftrightarrow \mathbf{p}_2$, one has $\mathbf{P}_- \to -\mathbf{P}_-$ and $\kappa \to -\kappa$. Thus, the parameters $f_\pm^J$ satisfy the conditions

$$f_+^J(-\kappa) = (-1)^S f_+^J(\kappa), \tag{24}$$

$$f_-^J(-\kappa) = (-1)^{S+1} f_-^J(\kappa). \tag{25}$$

IV. SDP FOR DPI BY TWO IDENTICALLY POLARIZED ELLIPTICAL PULSES

We present results for two time-delayed pulses with the same frequencies, numbers of cycles, and polarizations, but possibly different CEPs. Consequently, $J \equiv J_1 = J_2$ [see Eq. (10)] and $\mathbf{e} \equiv \mathbf{e}_1 = \mathbf{e}_2$ so that Eq. (9) becomes

$$\mathbf{e}' = J\,[1 + \exp(i\Phi)]\mathbf{e}. \tag{26}$$

Using Eqs. (18) and (26), the SDP (2) is

$$\begin{aligned}\mathcal{W}_{\xi,\ell} =& [2J\cos(\Phi/2)]^2\{|f_1|^2|\mathbf{e}\cdot\hat{\mathbf{p}}_1|^2 + |f_2|^2|\mathbf{e}\cdot\hat{\mathbf{p}}_2|^2\\ &+ 2\,\mathrm{Re}[f_1 f_2^*(\mathbf{e}\cdot\hat{\mathbf{p}}_1)(\mathbf{e}^*\cdot\hat{\mathbf{p}}_2)]\}.\end{aligned} \tag{27}$$

In Eq. (27) the geometric factors $|\mathbf{e}\cdot\hat{\mathbf{p}}_j|^2$ ($j = 1,2$), calculated using Eq. (5), reduce to

$$|\mathbf{e}\cdot\hat{\mathbf{p}}_j|^2 = \sin^2\theta_j(1 + \ell\cos 2\varphi_j)/2, \tag{28}$$

where θ_j and φ_j are the spherical angles of $\mathbf{p}_j$ in the coordinate frame whose x and z axes are along the vectors $\boldsymbol{\epsilon}$ and $\hat{\mathbf{k}}$, respectively (see Fig. 1). From Eq. (27) one sees that the major difference between the DPI angular distributions produced either by two pulses or by a single pulse lies in the Ramsey phase factor $\cos^2(\Phi/2)$, where Φ is given by Eq. (11). The SDP (27) is a general result that holds for any pair of elliptically polarized pulses, any energy partitioning, and any detection geometry.

A. Sensitivity of the SDP to the ellipticity

For two identical circularly polarized pulses we have $\xi_1 = \xi_2 = \xi$ and $\ell = 0$. Thus, from Eq. (5) we obtain

$$(\mathbf{e}\cdot\hat{\mathbf{p}}_j) = \sin\theta_j\exp(i\xi\varphi_j)/\sqrt{2}, \tag{29}$$

where $\xi = +1$ ($\xi = -1$) for right (left) circular polarization and θ_j,φ_j are the spherical angles of $\mathbf{p}_j$ ($j = 1,2$) in the coordinate frame defined above. Substituting Eqs. (28) and (29) into Eq. (27), an explicit expression for the SDP for any detection geometry and any energy sharing configuration is

$$\begin{aligned}\mathcal{W}_{\xi,0} =& 2[J\cos(\Phi/2)]^2\{|f_1|^2\sin^2\theta_1 + |f_2|^2\sin^2\theta_2\\ &+ 2\sin\theta_1\sin\theta_2\ \mathrm{Re}[f_1 f_2^* e^{i\xi(\varphi_1-\varphi_2)}]\}.\end{aligned} \tag{30}$$

For two identical linearly polarized pulses, $\eta = 0$, $\ell = 1$, and $\xi = 0$. Thus, the SDP (27) for any detection geometry and any energy-sharing configuration becomes

$$\begin{aligned}\mathcal{W}_{0,1} =& [2J\cos(\Phi/2)]^2[|f_1|^2\sin^2\theta_1\cos^2\varphi_1\\ &+ |f_2|^2\sin^2\theta_2\cos^2\varphi_2\\ &+ 2\,\mathrm{Re}(f_1 f_2^*)\sin\theta_1\sin\theta_2\cos\varphi_1\cos\varphi_2].\end{aligned} \tag{31}$$

B. Sensitivity of the SDP to the energy sharing

For ionization of an initial singlet state ($S = 0$), we have $f_1(p_2,p_1,\cos\beta) = f_2(p_1,p_2,\cos\beta)$ from Eq. (20). For unequal energy sharing (UES) configurations, Eq. (27) gives the SDP, $\mathcal{W}_{\xi,\ell}^{(\mathrm{UES})}$. However, for equal energy sharing (EES) configurations, one has $p_1 = p_2$ and $f_1 = f_2$. Hence, the above SDP (27) simplifies slightly in the conventional basis $\mathbf{p}_{1,2}$ for any ellipticity and any detection geometry to

$$\begin{aligned}\mathcal{W}_{\xi,\ell}^{(\mathrm{EES})} =& [2J\cos(\Phi/2)]^2\,|f_1|^2\{|\mathbf{e}\cdot\hat{\mathbf{p}}_1|^2 + |\mathbf{e}\cdot\hat{\mathbf{p}}_2|^2\\ &+ 2\,\mathrm{Re}[(\mathbf{e}\cdot\hat{\mathbf{p}}_1)(\mathbf{e}^*\cdot\hat{\mathbf{p}}_2)]\}.\end{aligned} \tag{32}$$

In contrast to Eq. (32), a compact form for the SDP for EES configurations can be obtained if one uses the PT amplitude (22) in the basis of Jacobi momenta, $\mathbf{P}_\pm$, since $f_-^J = 0$ at EES [see Eqs. (23) or (25)]. One obtains

$$\mathcal{W}_{\xi,\ell}^{(\mathrm{EES})} = [2J\cos(\Phi/2)]^2|f_+^J|^2|\mathbf{e}\cdot\hat{\mathbf{P}}_+|^2, \tag{33}$$

where $|\mathbf{e}\cdot\hat{\mathbf{P}}_+|^2$ is given by Eq. (28) upon replacing $\theta_j,\varphi_j \to \theta,\varphi$, where θ,φ are the spherical angles for $\hat{\mathbf{P}}_+$.

C. SDP dependence on the detection geometry

For two photoelectrons detected in the BTB geometry, $\hat{\mathbf{p}}_2 = -\hat{\mathbf{p}}_1$. Hence, the SDP (27) in the conventional $\mathbf{p}_{1,2}$ basis takes the following compact form for any ellipticity and energy-sharing configuration:

$$\mathcal{W}_{\xi,\ell}^{(\mathrm{BTB})} = [2J\cos(\Phi/2)]^2|f_1 - f_2|^2|\mathbf{e}\cdot\hat{\mathbf{p}}_1|^2. \tag{34}$$

Similar closed-form expressions for the SDP in the $\mathbf{p}_\pm$ basis [see A_1 (14)] or in the $\mathbf{P}_\pm$ basis [see A_1 (22)] can be derived using the fact that $\hat{\mathbf{p}}_+ = 0$ for the BTB geometry:

$$\mathcal{W}_{\xi,\ell}^{(\mathrm{BTB})} = [2J\cos(\Phi/2)]^2|f_-|^2|\mathbf{e}\cdot\hat{\mathbf{p}}_-|^2, \tag{35}$$

where $\mathbf{p}_-$ and $\mathbf{P}_\pm$ are all collinear in this case since $\mathbf{P}_+ = (p_1 - p_2)\mathbf{p}_-$ and $\mathbf{P}_- = [(p_1 + p_2)/2]\mathbf{p}_-$. Clearly, Eq. (34) or Eq. (35) shows that $\mathcal{W}_{\xi,\ell}^{(\mathrm{BTB})} = 0$ for EES ($f_1 = f_2$) and BTB emission of electrons in DPI of a singlet state.

D. Numerical results and analyses for the detection geometries in Figs. 1(b) and 1(c)

Note that the parametrization (32) of the SDP for EES configurations written in terms of Jacobi momenta is similar to that for the BTB emission geometry; see Eqs. (33), (35). Using Eq. (28), the SDP for both EES and BTB cases can be presented in a unified form:

$$\mathcal{W}_{\xi,\ell} = 2[J\cos(\Phi/2)]^2\,|\Upsilon(p_1,p_2,\beta)|^2\sin^2\theta(1+\ell\cos 2\varphi). \tag{36}$$

For the BTB geometry, (θ,φ) are the spherical angles defining the emission direction of the electrons, and the newly introduced dynamical parameter Υ is defined by

$$\Upsilon(p_1,p_2,\beta=\pi) = f_- = f_1(p_1,p_2,-1) - f_1(p_2,p_1,-1). \tag{37}$$

For the EES configuration, (θ,φ) are the spherical angles of the Jacobi vector $\mathbf{P}_+$, and the parameter Υ is

$$\Upsilon(p_1,p_1,\beta) = f_+p_+ = 2f_1(p_1,p_1,\cos\beta)\cos(\beta/2). \tag{38}$$

For the detection geometries defined by Figs. 1(b) and 1(c), the polar angle $\theta=\pi/2$ and φ is the azimuthal angle of the detected momentum $\mathbf{p}_2$ (or of $\mathbf{P}_+$ in the EES scheme). For the orthogonal detection geometry in Fig. 1(c), $\beta=\pi/2$, and $\Upsilon(p_1,p_1,\pi/2)=\sqrt{2}\,f_1(p_1,p_1,0)$.

A key result of the PT formula (36) for corotating pulses for any β-fixed EES detection geometry [see, e.g., Fig. 1(c)] or for the in-plane BTB geometry [see Fig. 1(b)] is that the φ dependence of the SDP (36) is determined by the degree of linear polarization ℓ.

To demonstrate numerically this PT prediction, the dependence of the SDP on the degrees of circular polarization (ξ_1,ξ_2) for the $\mathbf{P}_-$ or $\mathbf{P}_+$ momentum distributions produced by a pair of identical time-delayed attosecond pulses is shown in Fig. 2 for an UES configuration and in Fig. 3 for an EES configuration. Specifically, in Fig. 2, the two electrons are emitted BTB in the polarization plane [see Fig. 1(b)] and share unequally the excess energy $0.1\leqslant E\leqslant 33$ eV (determined by the broad bandwidth of the attosecond pulses) in the proportion 17.5% : 82.5%. In Fig. 3, the two electrons have the same energy and are emitted in an orthogonal scheme such that $\mathbf{p}_1$ is detected along the laser propagation direction $\hat{\mathbf{k}}$, whereas $\mathbf{p}_2$ is detected in the polarization plane [see Fig. 1(c)]. In Figs. 2 and 3, two time delays are considered: $\tau=0$ and $\tau=275$ as. Note that all results in this paper are produced by attosecond pulses having a carrier frequency of $\omega=90$ eV, an intensity of $I=50$ TW/cm^2, a cos^2 envelope profile, and $N=6$ optical cycles, which corresponds to a pulse duration of $T\simeq 275$ as.

Consider first the case in which the two pulses, each with zero CEP, arrive at the target simultaneously (i.e., $\tau=0$). For two linearly polarized pulses, $\ell=1$, and hence, regardless of the energy sharing, the SDP (36) depends on φ: its polar angle plots in the polarization plane $(\theta=\pi/2)$ have symmetric dipole patterns [$\propto\cos^2\varphi$]. Our TDSE results confirm this prediction, as shown in Fig. 2(a) for an UES configuration and in Fig. 3(a) for an EES configuration. For two circularly

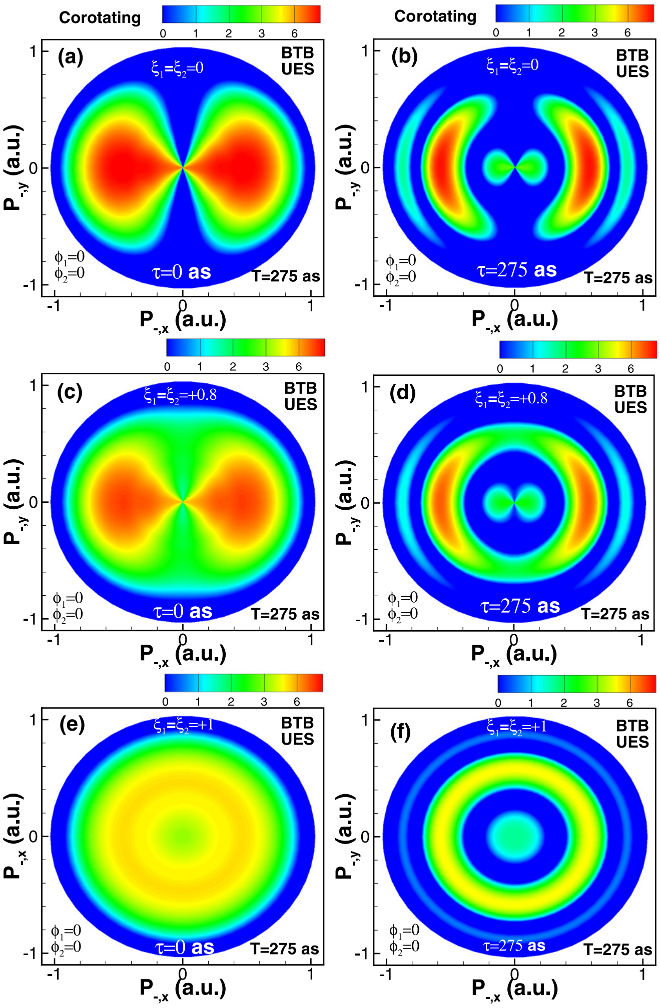

FIG. 2. TDSE results for the electron-pair momentum distribution, $\mathcal{W}_{\xi,\ell}(\mathbf{P}_-)$ [calculated using Eq. (1) and analyzed in the text using PT Eqs. (36) and (37)], produced in DPI of the He atom by two corotating identical attosecond pulses delayed in time by $\tau=0$ (left panels) and $\tau=275$ as (right panels) for three degrees of circular polarization: (a), (b) $\xi_{1,2}=0$; (c), (d) $\xi_{1,2}=+0.8$; (e), (f) $\xi_{1,2}=+1$. The two electrons are emitted BTB in the polarization plane [Fig. 1(b)] and share unequally the excess energy $0.1\leqslant E\leqslant 33$ eV in the proportion 17.5% : 82.5%. Each pulse has a carrier frequency $\omega=90$ eV, an intensity $I=50$ TW/cm^2, a cos^2 envelope profile, $N=6$ optical cycles, and a duration of $T\simeq 275$ as. The magnitudes of the SDPs $\mathcal{W}_{\xi,\ell}(\mathbf{P}_-)$ (in units of 10^{-7} a.u.) are indicated by the color scales in each panel.

polarized pulses, one has $\eta=\pm1$, $\xi=\pm1$, and $\ell=0$. Hence, the SDP (36) for any energy sharing is independent of φ: its polar angle plots in the polarization plane have circularly symmetric patterns, as confirmed by our TDSE results in Fig. 2(e) for an UES configuration and in Fig. 3(e) for an EES configuration. For two identical elliptically polarized pulses, one has $-1<\eta<+1$, $-1<\xi<+1$, and $0<\ell<1$. Hence, the SDP (36) for any energy sharing depends on φ: its polar angle plots in the polarization plane are expected to be a mixture of symmetric-dipole and circularly symmetric patterns as the SDP (36) is $\propto 1+\ell\cos(2\varphi)$. This prediction is confirmed by our TDSE results for pulses with $\xi=+0.8$,

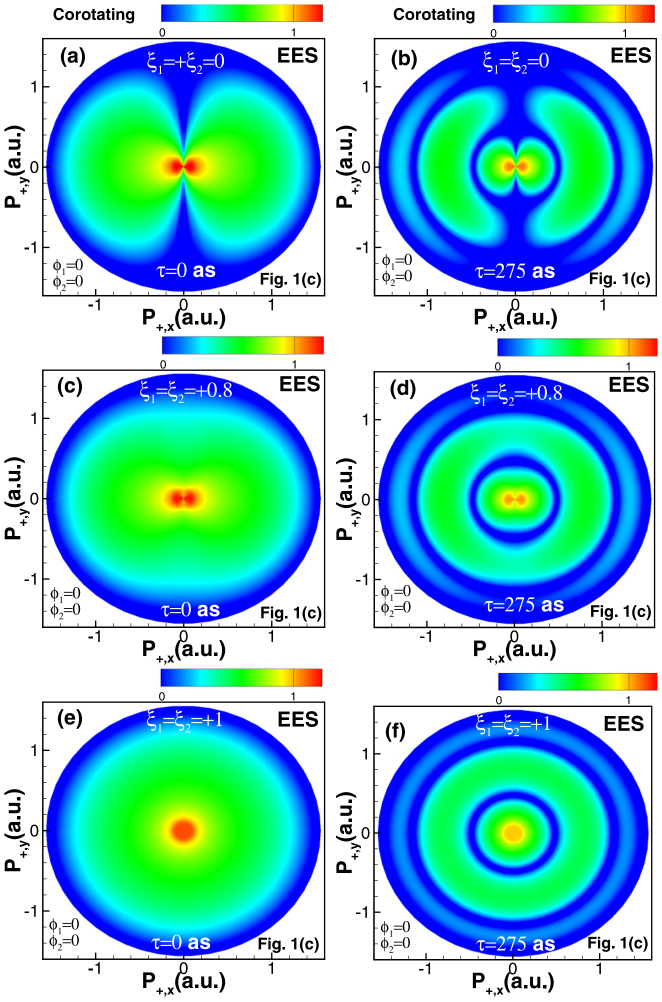

FIG. 3. TDSE results for the electron-pair momentum distribution, $\mathcal{W}_{\xi,\ell}(\mathbf{P}_+)$ [calculated using Eq. (1) and analyzed in the text using PT Eqs. (36) and (38)], produced in DPI of the He atom by two corotating identical attosecond pulses delayed in time by $\tau = 0$ (left panels) and $\tau = 275$ as (right panels) for three degrees of circular polarization: (a), (b) $\xi_{1,2} = 0$; (c), (d) $\xi_{1,2} = +0.8$; (e), (f) $\xi_{1,2} = +1$. The two electrons are emitted in the EES orthogonal detection geometry [Fig. 1(c)]. The pulse parameters are the same as in Fig. 2. The magnitudes of the SDPs $\mathcal{W}_{\xi,\ell}(\mathbf{P}_+)$ (in units of 10^{-5} a.u.) are indicated by the color scales in each panel.

as shown in Fig. 2(c) for an UES configuration and in Fig. 3(c) for an EES configuration. For $\tau = 0$, owing to the dependence of the SDP (36) on the relative phase Φ (12), we confirm numerically (not shown) that for relative CEPs $\phi_{12} = \pm(2n+1)\pi$, where n is an integer, one can turn off the DPI process, i.e., the SDP vanishes. Conversely, for two identical pulses (i.e., with $\phi_{12} = 0$), the case of $\tau = 0$ is equivalent to DPI by a single pulse having twice the field strength.

Consider now the case in which the two pulses, each with zero CEP, are delayed in time by $\tau = 275$ as. For two linearly polarized pulses ($\ell = 1$), both the $\mathbf{P}_-$ momentum distribution shown in Fig. 2(b) for an UES scheme and the $\mathbf{P}_+$ momentum distribution shown in Fig. 3(b) for an EES scheme exhibit a superposition of both a symmetric dipole pattern [as in Figs. 2(a) and 3(a) for $\tau = 0$] and Ramsey interference fringes. These interference fringes are the signature in the SDP (36) of the phase $\Phi = (E + E_g)\tau$ [see Eq. (12)] as the kinetic energy E of the two continuum electrons varies over the bandwidth of the laser pulses. For two circularly polarized pulses ($\ell = 0$), our TDSE results in Fig. 2(f) for the UES scheme and in Fig. 3(f) for the EES scheme show a Ramsey interference pattern similar to Newton's rings, i.e., maxima and minima along the radial direction in momentum space. (Note that the interference patterns in Figs. 2(f) and 3(f) are similar to the patterns found in interference of two identical vortex optical beams having an orbital angular momentum of unity [46].) For two elliptically polarized pulses, each with $\ell = 0.6$, our TDSE results in Fig. 2(d) for the UES case and in Fig. 3(d) for the EES case exhibit Ramsey interference patterns that are intermediate between the axially symmetric interference fringes of the linear polarization case and the circularly symmetric interference fringes (or Newton's rings) of the circular polarization case.

V. SDP FOR DPI BY TWO OPPOSITELY POLARIZED ELLIPTICAL PULSES

For a pair of oppositely polarized elliptical pulses we have $\mathbf{e} \equiv \mathbf{e}_1 = \mathbf{e}_2^*$, and the expression (9) for the effective polarization vector $\mathbf{e}'$ becomes

$$\mathbf{e}' = J[\mathbf{e} + \mathbf{e}^* \exp(i\Phi)]. \tag{39}$$

In order to evaluate the SDP in Eq. (2) in the conventional momentum basis, $\mathbf{p}_{1,2}$, we must evaluate $|A_1|^2$ using Eq. (18). Taking Eq. (5) into account, we note the following expressions for the various scalar products involving polarization vectors and electron momentum unit vectors that occur in the expression for $|A_1|^2$:

$$(\hat{\mathbf{p}} \cdot \mathbf{e})^2 = \frac{\sin^2\theta}{2}(\ell + \cos 2\varphi + i\xi \sin 2\varphi), \tag{40}$$

$$(\mathbf{e}^* \cdot \hat{\mathbf{p}}_1)(\mathbf{e} \cdot \hat{\mathbf{p}}_2) = \tfrac{1}{2}\sin\theta_1 \sin\theta_2[\ell\cos(\varphi_1+\varphi_2) + \cos(\varphi_1-\varphi_2) - i\xi\sin(\varphi_1-\varphi_2)], \tag{41}$$

$$(\mathbf{e} \cdot \hat{\mathbf{p}}_1)(\mathbf{e} \cdot \hat{\mathbf{p}}_2) = \tfrac{1}{2}\sin\theta_1 \sin\theta_2[\ell\cos(\varphi_1-\varphi_2) + \cos(\varphi_1+\varphi_2) + i\xi\sin(\varphi_1+\varphi_2)]. \tag{42}$$

Using Eqs. (18) and (39)–(42), the SDP in Eq. (2) for DPI by a pair of oppositely polarized elliptical pulses is

$$\frac{\mathcal{W}_{\xi,-\xi}}{J^2} = \sum_{j=1}^{2} |f_j|^2 \sin^2\theta_j \big\{1 + \ell\cos 2\varphi_j + \xi\sin\Phi\sin 2\varphi_j + (\ell + \cos 2\varphi_j)\cos\Phi\big\} + 2\,\mathrm{Re}(f_1^* f_2)\sin\theta_1\sin\theta_2 \times \{(\ell + \cos\Phi)\cos(\varphi_1+\varphi_2) + \xi\sin\Phi\sin(\varphi_1+\varphi_2) + (1 + \ell\cos\Phi)\cos(\varphi_1-\varphi_2)\}. \tag{43}$$

Equation (43) for the SDP is general and applies for any counterrotating pulse ellipticities $\xi \equiv \xi_1 = -\xi_2$ (corresponding to $\ell \equiv \ell_1 = \ell_2$), for any energy-sharing scheme, and for any detection geometry. In Secs. V A and V B below, we predict that for the detection geometries in Fig. 1, Eq. (43) simplifies and leads to kinematical spiral vortices. The resulting formulas are then used to interpret our numerical results in Secs. V C and V D.

A. Detection geometries for producing spiral vortices using oppositely circularly polarized pulses

For the case of counterrotating, circularly polarized pulses, for which $\ell = 0$, the SDP (43) reduces to

$$\frac{\mathcal{W}_{\xi,-\xi}}{2J^2} = \sum_{j=1}^{2} |f_j|^2 \big[\sin\theta_j \cos(\varphi_j - \xi\Phi/2)\big]^2 + \mathrm{Re}\big(f_1^* f_2\big) \times \sin\theta_1 \sin\theta_2 [\cos(\varphi_1 - \varphi_2) + \cos(\varphi_1 + \varphi_2 - \xi\Phi)]. \quad (44)$$

Equation (44) simplifies, taking a fully factorized form, when the electron momenta $\mathbf{p}_1$, $\mathbf{p}_2$ and the pulse propagation direction $\hat{\mathbf{k}}$ are all in the same plane, as shown in Fig. 1(a). As this scattering plane rotates with the angle $\varphi \equiv \varphi_2$ about the $\hat{\mathbf{k}}$ axis, two detection configurations can be defined in terms of the azimuthal angle of $\mathbf{p}_1$: (i) configuration *SHP* (in which $\mathbf{p}_1$, $\mathbf{p}_2$ are in the *same half plane*), i.e., $\varphi_1 = \varphi$ and $\beta = |\theta_1 - \theta_2|$; and (ii) configuration *OHP* (in which $\mathbf{p}_1$, $\mathbf{p}_2$ are in *opposite half planes*), i.e., $\varphi_1 = \varphi + \pi$ and $\beta = \theta_1 + \theta_2$. The SDP (44) for the SHP and OHP configurations has the factorized form

$$\mathcal{W}_{\xi,-\xi}(\theta_1,\theta_2,\varphi_1) = 2J^2 |f_1 \sin\theta_1 \pm f_2 \sin\theta_2|^2 \times \cos^2(\varphi - \xi\Phi/2), \quad (45)$$

where the $+$ $(-)$ sign in the squared modulus is for the SHP (OHP) configuration, and right-left (left-right) circularly polarized pulses are specified by $\xi = +1$ $(\xi = -1)$.

For BTB electron emission in Fig. 1(a), $\theta_1 = \pi - \theta_2$ and the SDP (45) for the configuration OHP for any energy-sharing scheme reduces to

$$\mathcal{W}_{\xi,-\xi} = 2J^2 |f_1 - f_2|^2 \sin^2\theta_2 \cos^2(\varphi - \xi\Phi/2). \quad (46)$$

For EES, the SDP (46) vanishes since $f_1 = f_2$ [see Eq. (20)]. For UES and $\theta_1 = \theta_2 = \pi/2$, Eq. (46) gives the SDP for the BTB geometry in the polarization plane defined in Fig. 1(b).

For the detection geometry in Fig. 1(a) in which $\mathbf{p}_1 || \hat{\mathbf{k}}$, we have $\theta_1 = 0$. Thus, for any energy partitioning of the two electrons, the SDP (45) becomes

$$\mathcal{W}_{\xi,-\xi} = 2J^2 |f_2|^2 \sin^2\theta_2 \cos^2(\varphi - \xi\Phi/2). \quad (47)$$

For $\theta_2 = \pi/2$ in Fig. 1(a) and for the case of EES, Eq. (47) provides the SDP for the out-of-plane orthogonal geometry defined in Fig. 1(c).

Two important aspects of the SDPs (45), (46), and (47) should be noted. First, the dynamical amplitudes $f_{1,2}$ have no angular dependence, as $\beta \equiv \cos^{-1}(\hat{\mathbf{p}}_1 \cdot \hat{\mathbf{p}}_2)$ is kept fixed for the detection schemes shown in Fig. 1. Second, the angular dependence of each of these SDPs is given by the factor $\cos^2(\varphi - \xi\Phi/2)$, which has its maximum when

$$\varphi^{\max} = \xi\Phi/2 + \pi n, \quad n = 0, \pm 1, \pm 2, \ldots, \quad (48)$$

and vanishes when

$$\varphi^{\text{zero}} = \xi\Phi/2 + \pi(n + 1/2), \quad n = 0, \pm 1, \pm 2, \ldots. \quad (49)$$

Equations (48) and (49) thus define kinematical Fermat spiral vortices in the polar coordinate plane φ, p_2.

The spiral patterns predicted above for counterrotating, circularly polarized attosecond pulses in the conventional momentum basis of $\mathbf{p}_{1,2}$ can also be observed when measuring the SDP as a function of Jacobi momenta, $\mathbf{P}_{\pm}$. For each of the detection geometries in Fig. 1, using the amplitude (22) in the $\mathbf{P}_{\pm}$ basis, the SDPs can be derived. The resulting expressions for the SDPs in the $\mathbf{P}_{\pm}$ basis can be simply obtained from the above results (43)–(47) in the $\mathbf{p}_{1,2}$ basis, as follows: (i) θ_1,φ_1 (θ_2,φ_2) for $\mathbf{p}_1$ $(\mathbf{p}_2)$ should be understood as the spherical angles of the momentum $\mathbf{P}_+$ $(\mathbf{P}_-)$; and (ii) the dynamical parameters (f_1, f_2) should be replaced respectively by (f_+^J, f_-^J), defined in Eq. (23).

B. SDP for DPI by oppositely elliptically polarized pulses in the Jacobi momentum basis

For the detection geometries in Figs. 1(b) and 1(c), an expression for the SDP for DPI by oppositely elliptically polarized pulses in the Jacobi momentum basis $\mathbf{P}_{\pm}$ can be derived using the amplitude (22). For oppositely elliptically polarized pulses, $\mathbf{e}_1 = \mathbf{e}_2^*$, $\ell \equiv \ell_1 = \ell_2$, and $\xi \equiv \xi_1 = -\xi_2$. The result is

$$\mathcal{W}_{\xi,-\xi} = J^2 |\Upsilon|^2 \sin^2\theta \big[2\cos^2(\varphi - \hat{\xi}\Phi/2) + (\xi - \hat{\xi})\sin\Phi \sin 2\varphi + \ell(\cos\Phi + \cos 2\varphi)\big], \quad (50)$$

where $\hat{\xi} \equiv \xi/|\xi|$; θ,φ are the spherical angles of either the momentum $\mathbf{P}_-$ [Fig. 1(b)] or $\mathbf{P}_+$ [Fig. 1(c)]; and Υ is defined by (37) for the BTB geometry or by (38) for the EES scheme. Note that the dynamical parameter Υ applies for any two-pulse polarization case; i.e., its measurement in one polarization case determines it in all others.

C. Numerical results and analyses for the detection geometries in Figs. 1(b) and 1(c)

The numerical results confirming these PT predictions for the two-electron momentum distributions produced in DPI of He by time-delayed, oppositely elliptically polarized attosecond pulses are shown in Fig. 4 (for a time delay $\tau = 0$) and in Fig. 5 (for a time delay $\tau = 275$ as). In each figure, results are given for both the UES BTB in-plane detection scheme shown in Fig. 1(b) and for the EES out-of-plane detection scheme shown in Fig. 1(c). For each τ, we discuss below the sensitivity of the two-electron momentum distributions to the ellipticities of the pulse pair. In Figs. 4 and 5 the CEPs of the pulses are zero (i.e., $\phi_1 = \phi_2 = 0$) and, in the UES case, the energy sharing is fixed. However, in Fig. 6 we analyze the sensitivity of the angular distributions to both the CEPs of the pulses and to the energy sharing of the ionized electrons.

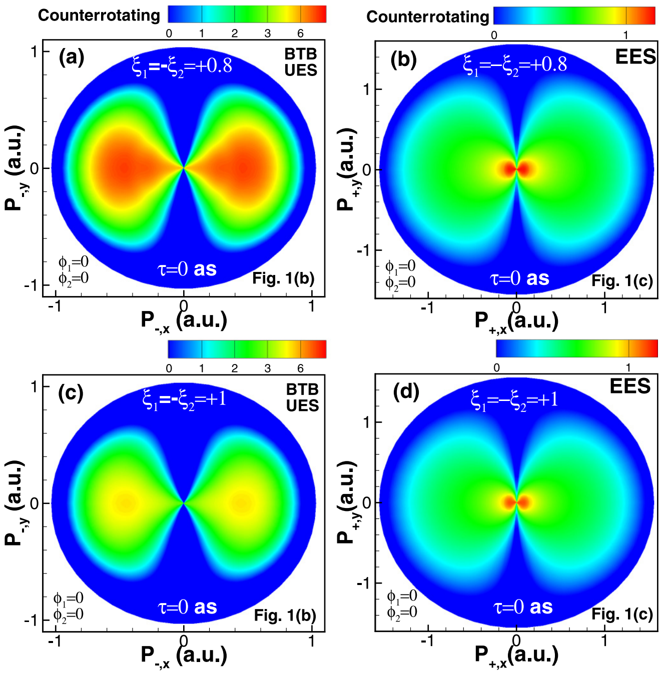

FIG. 4. TDSE results for the electron-pair momentum distributions produced by a pair of oppositely elliptically polarized pulses delayed in time by $\tau = 0$. Panels (a) and (c) show $\mathcal{W}_{\xi,\ell}(\mathbf{P}_-)$ for the BTB UES detection geometry in Fig. 1(b) [calculated using Eq. (1) and analyzed in the text using PT Eqs. (50) or (46)]; panels (b) and (d) show $\mathcal{W}_{\xi,\ell}(\mathbf{P}_+)$ for the orthogonal EES detection geometry in Fig. 1(c) [calculated using Eq. (1) and analyzed in the text using PT Eqs. (50) or (47)]. Top row: $\xi_1 = -\xi_2 = +0.8$; bottom row: $\xi_1 = -\xi_2 = +1$. The magnitudes of the SDPs are indicated by the color scales in each panel, in units of 10^{-7} a.u. in the left column and in units of 10^{-5} a.u. in the right column.

We consider first the case of counterrotating attosecond pulses with $\tau = 0$. Our TDSE results for elliptically polarized pulses with $\xi_1 = -\xi_2 = +0.8$ and for $\xi_1 = -\xi_2 = +1$ are shown in Fig. 4. For oppositely elliptically polarized pulses for which $\phi_{12} = 0$ and $\tau = 0$, PT indicates that the resulting zero value of the phase factor Φ (11) eliminates any angular distortion from the ellipticity dependence of the SDP (50). Specifically, for any circular polarization degree $\xi \equiv \xi_1 = -\xi_2$, the SDP (50) has the same symmetric dipole pattern [$\propto \cos^2\varphi$]; only its magnitude [$\propto 2(1+\ell)$] depends on ℓ. These PT predictions are confirmed numerically for our two detection geometries for any circular polarization degree ξ, as shown in Fig. 4 for $\xi \neq 0$ and in Figs. 2(a) and 3(a) for $\xi = 0$. For nonzero relative CEP ϕ_{12}, $\Phi = \phi_{12}$ and the PT formula (50) shows that the SDP is sensitive to the circular polarization degree ξ of the pulse pair. This is demonstrated numerically in Fig. 6(a) for the angular distributions produced by two oppositely elliptically polarized pulses ($\xi_1 = -\xi_2 = +0.8$) for $\phi_{12} = 0$ and $\phi_{12} = \pi/2$. One sees that the ϕ_{12} sensitivity affects only slightly the shape of the angular distribution but has a strong effect on its magnitude. These results indicate the importance of controlling the relative CEP of the two counterrotating elliptically polarized pulses. For a pair of oppositely circularly polarized pulses, varying ϕ_{12} results in a

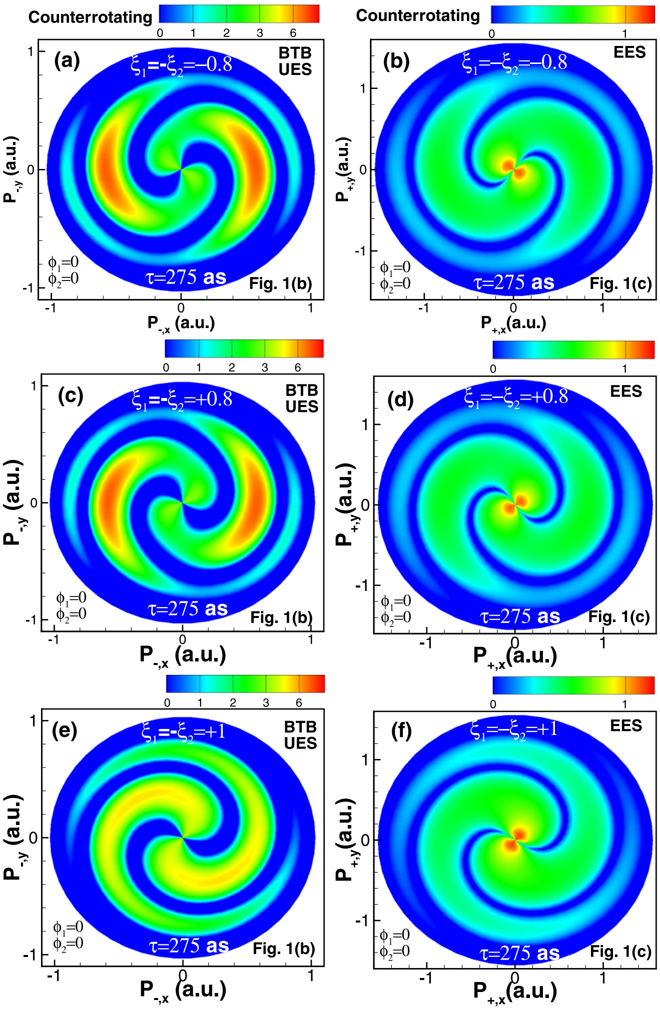

FIG. 5. Same as Fig. 4 for two oppositely elliptically polarized pulses delayed by $\tau = 275$ as. Top row: $\xi_1 = -\xi_2 = -0.8$; middle row: $\xi_1 = -\xi_2 = +0.8$; bottom row: $\xi_1 = -\xi_2 = +1$.

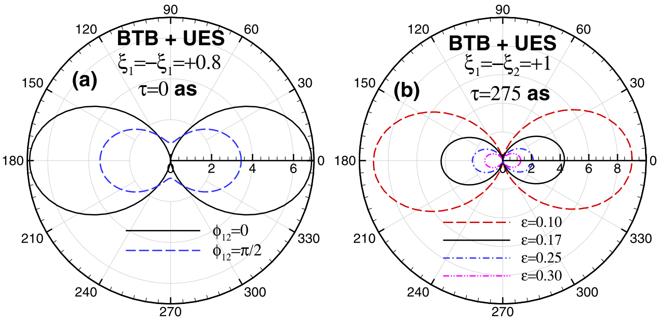

FIG. 6. Dependence of the TDSE results for the DPI angular distribution (1) (in units of 10^{-7} a.u.) on (a) the relative CEP and (b) the energy-sharing configuration for electrons emitted BTB in the polarization plane [Fig. 1(b)]. In (a), two values of the relative CEP ($\phi_{12} = 0,\pi/2$) are considered for right-left elliptically polarized pulses ($\xi_1 = -\xi_2 = +0.8$) delayed in time by $\tau = 0$ and with fixed degree of energy sharing $\varepsilon = 17.5\%$, where $\varepsilon = E_1/E$ with $E = E_1 + E_2 = 11$ eV. In (b), results are shown for four values of ε (see the legend) for right-left circularly polarized pulses delayed in time by $\tau = 275$ as. Other pulse parameters are the same as in the caption of Fig. 2.

global rotation of the pattern of the momentum distribution, as found numerically (not shown) and predicted by PT formula (46) or (47) (see also Refs. [44,65]). For a pair of linearly polarized pulses, PT formula (31) shows that varying $\phi_{12} = \Phi$ affects only the magnitude of the momentum distribution and not its shape.

Consider now the case of counterrotating pulses delayed in time by $\tau = 275$ as, with each pulse having the same zero CEP. Figures 5(a), 5(c) and 5(e) show the $\mathbf{P}_-$ distributions for our BTB UES scheme [Fig. 1(b)] and Figs. 5(b), 5(d) and 5(f) show the $\mathbf{P}_+$ distributions for our orthogonal EES scheme [Fig. 1(c)]. The top, middle, and bottom rows of Fig. 5 show, respectively, the momentum distributions produced by left-right elliptically polarized pulses with $\xi_1 = -\xi_2 = -0.8$, right-left elliptically polarized pulses with $\xi_1 = -\xi_2 = +0.8$, and right-left circularly polarized pulses with $\xi_1 = -\xi_2 = +1$. For all cases shown in Fig. 5, we observe two-start spiral vortex patterns in the polarization plane, distorted (for $0 < \xi < 1$) or not (for $\xi = 1$) depending on the degree of circular polarization $\xi = \xi_1 = -\xi_2$. For elliptically polarized pulses, the distortion in the vortex pattern originates from the two terms in the second line of Eq. (50), which vanish for oppositely circularly polarized pulses. For left-right handedness of the two pulses, the spiral patterns have a clockwise rotation [see Figs. 5(a) and 5(b)], while for right-left handedness of the two pulses they have a counterclockwise rotation [see Figs. 5(c)–5(f)]. These features of the TDSE results for the SDPs are described well by the PT Eqs. (46) and (47) applicable to the two detection geometries defined in Figs. 1(b) and 1(c), respectively, together with Eqs. (48) and (49) describing the momentum locations of the maxima and minima of the spiral vortex patterns. As in Fig. 3 of Ref. [44] for the corresponding single photoionization of He, it is found that time delays of several hundred attoseconds are necessary to observe well-defined vortex patterns. Also, the broad bandwidth $\Delta\omega$ of attosecond pulses is necessary to observe the spiral patterns; specifically, the time delay and the bandwidth should satisfy $2\pi/\tau < \Delta\omega$. These findings stem from the definition of Φ in Eqs. (11) or (12) and the common factor $\cos^2(\varphi - \xi\Phi/2)$ appearing in both of the SDP Eqs. (46) and (47). For fixed φ, as Φ increases (with either electron energy E or pulse time delay τ) the factor $\cos^2(\varphi - \xi\Phi/2)$ oscillates. For fixed time delay, the bandwidth of the pulses determines the range over which E varies, with the phase change being larger for larger τ. In the Supplemental Material [66], we provide an animation showing the evolution with time delay τ over the range $0 \leqslant \tau \leqslant 550$ as of the vortex pattern in Fig. 5(e) for the case $\xi_1 = -\xi_2 = +1$; a second animation for the case $\xi_1 = -\xi_2 = -1$ is also given.

In Figs. 4, 5, and 6(a) the energy sharing of the two photoelectrons is fixed to $\varepsilon = 17.5\%$, where $\varepsilon = E_1/E$; in Fig. 6(b) we show results for four different values of the energy sharing for the in-plane BTB UES detection geometry [Fig. 1(b)] at the *fixed* excess energy $E = 11$ eV. In each case the pulse pair is right-left circularly polarized with a time delay of $\tau = 275$ as. One sees that the DPI signal is large for very asymmetric UES schemes, but decreases rapidly as one approaches equal energy sharing. The effect of varying the energy sharing on the $\mathbf{P}_-$ distributions (not shown) is similar: namely, the magnitude of the SDP is significantly suppressed as one approaches equal energy sharing.

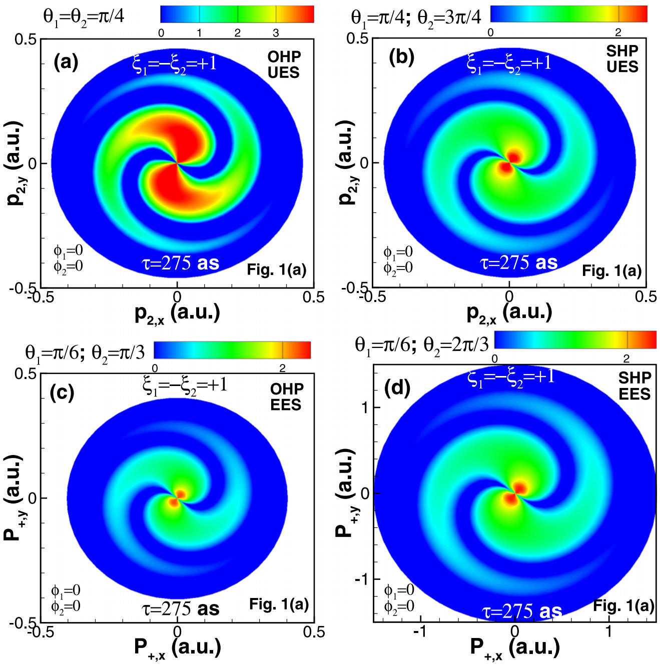

FIG. 7. Momentum distributions for DPI of He by right-left circularly polarized pulses delayed in time by $\tau = 275$ as for four out-of-plane detection geometries [see Fig. 1(a)]: (a) UES scheme for opposite half plane (OHP) emission of electrons with $\theta_1 = \theta_2 = \pi/4$, $\varphi_2 = \pi + \varphi$; (b) UES scheme with electrons emitted in the same half plane (SHP) with $\theta_1 = \pi/4$, $\theta_2 = 3\pi/4$, $\varphi_2 = \varphi$; (c) EES scheme for OHP emission of electrons with $\theta_1 = \pi/6$, $\theta_2 = \pi/3$, $\varphi_2 = \pi + \varphi$; and (d) EES scheme SHP emission of electrons with $\theta_1 = \pi/6$, $\theta_2 = 2\pi/3$, $\varphi_2 = \varphi$. The color scale shows the SDPs in units of (a) 10^{-9} a.u., (b) 10^{-5} a.u., (c) 10^{-6} a.u., and (d) 10^{-5} a.u.

D. Numerical results and analyses for four out-of-plane detection geometries in Fig. 1(a)

For four general out-of-plane detection geometries [in which both electrons are emitted out of the polarization plane, as shown in Fig. 1(a)], TDSE results for the DPI momentum distributions produced by right-left circularly polarized attosecond pulses delayed in time by $\tau = 275$ as are shown in Fig. 7. These include two detection schemes for OHP emission of electrons (in which $\beta = \theta_1 + \theta_2$) and two detection schemes for SHP emission of electrons (in which $\beta = |\theta_1 - \theta_2|$). For an UES configuration with a degree of energy sharing of $\varepsilon = E_1/E = 17.5\%$, the $\mathbf{p}_2$ distribution for an OHP detection geometry defined by $\theta_1 = \theta_2 = \pi/4$ and $\varphi_2 = \varphi_1 + \pi$ is displayed in Fig. 7(a), while the $\mathbf{p}_2$ distribution for a SHP detection geometry defined by $\theta_1 = \pi/4$, $\theta_2 = 3\pi/4$, and $\varphi_2 = \varphi_1$ is shown in Fig. 7(b). Likewise, for an EES configuration, the $\mathbf{P}_+$ distribution for an OHP detection geometry defined by $\theta_1 = \pi/6$, $\theta_2 = \pi/3$, and $\varphi_2 = \varphi_1 + \pi$ is plotted in Fig. 7(c), while the $\mathbf{P}_+$ distribution for a SHP detection geometry defined by $\theta_1 = \pi/6$, $\theta_2 = 2\pi/3$, and $\varphi_2 = \varphi_1$ is shown in Fig. 7(d). Of note is that for the detection schemes in Figs. 7(a) and 7(b), the SDPs vanish for an EES configuration, which is consistent with the PT formula (45). Clearly, one sees that the momentum distributions in Figs. 7(a)–7(d) for all these out-of-plane detection geometries

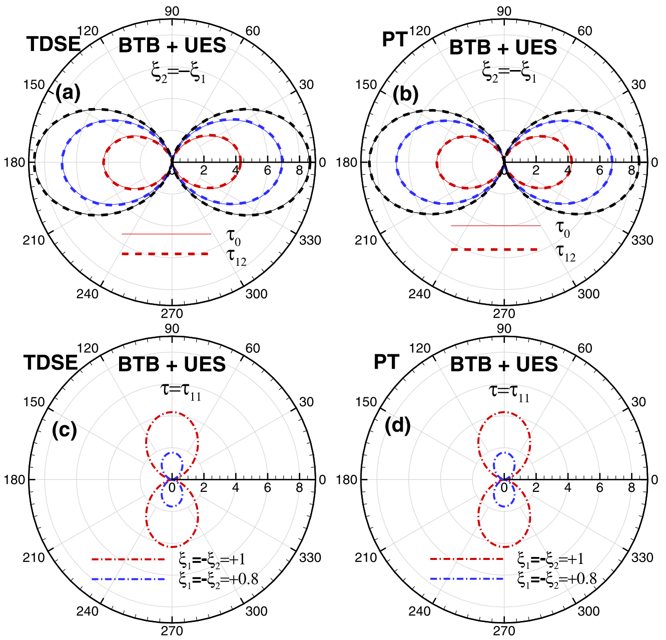

FIG. 8. Time-delay periodicity of two-electron angular distributions (in units of 10^{-7} a.u.) for the in-plane BTB detection geometry [Fig. 1(b)] at *fixed* excess energy $E = 11$ eV and energy sharing $\varepsilon = E_1/E = 17.5\%$ produced by a pair of right-left elliptically polarized attosecond pulses. In each row, TDSE results on the left are compared with PT results on the right and for each time delay, results are given for three degrees of circular polarization: $\xi_1 = -\xi_2 = +1$ (red lines), $+0.8$ (blue lines), and 0 (black lines). In (a), (b), results are shown for two *even* time delays: τ_0 (solid lines) and τ_{12} (dashed lines), where $\tau_n = n\pi/\omega$. In (c), (d) results are given for one *odd* time delay $\tau = \tau_{11}$. [Note that at $\tau = \tau_{11}$ for $\xi_1 = -\xi_2 = 0$, the SDP (31) vanishes, as discussed in the text.] Other pulse parameters are as in Fig. 2.

exhibit a *two-start* spiral vortex structure, as expected from the PT formula (45).

VI. TIME-DELAY PERIODICITY AND CONTROL OF THE ANGULAR DISTRIBUTIONS

The time-delay periodicity of the two-electron angular distributions for the in-plane BTB emission geometry [Fig. 1(b)] is demonstrated in Fig. 8 for a *fixed* excess energy $E = \omega - E_g = 11$ eV with an energy-sharing of $\varepsilon = E_1/E = 17.5\%$. Our TDSE results in Figs. 8(a) and 8(c) are compared with our PT results in Figs. 8(b) and 8(d), respectively. The numerical PT results displayed in Figs. 8(b) and 8(d) are obtained using Eqs. (31), (46), and (50), in which the dynamical parameter $f_-(p_1,p_2,\cos\beta)$ for $\beta = \pi$ is extracted numerically from *ab initio* TDSE calculations by a *single* pulse that can be either circularly, elliptically, or linearly polarized. Results are given for three values of $\xi_1 = -\xi_2 = 0, +0.8, +1$.

From the definition of the phase Φ (12), for fixed relative CEP ϕ_{12} and energy E, the two-electron angular distribution produced by a pair of polarized pulses is unchanged for time delays of $\tau_n = n\pi/(E + E_g)$ with n an even integer, as may be seen for our β-fixed UES and EES geometries from the PT Eqs. (50) for elliptically polarized pulses, (46) for circularly polarized pulses, and (31) for linearly polarized pulses. Regardless of the ellipticities of the pulses, the numerical evaluation of these PT formulas, shown in Fig. 8(b), confirms this analytical PT prediction that the angular distributions for τ_0 and τ_{12} are identical. Moreover, our *ab initio* TDSE results in Fig. 8(a) show that for each of the three ellipticities shown, the results for the two even time delays coincide.

For time delays τ_n with odd integer n, the PT formula (46) and (12) for a pair of circularly polarized pulses predict the angular distributions to be shifted by $\pi/2$ with respect to those for even-integer n. This is demonstrated by our TDSE and PT results in Fig. 8(c) and Fig. 8(d), respectively, for $\tau = \tau_{11}$. This result is valid for any value of the relative CEP ϕ_{12}. For a pair of linearly polarized pulses, the PT formulas (31) and (12) predict that the axis of the dipolar angular distribution does not change for time delays τ_n with odd integer n. However, the magnitude of the angular distribution is $\propto \sin^2(\phi_{12}/2)$, so that for $\phi_{12} = 0$ it vanishes. Our numerical TDSE results for $\phi_{12} = 0$ and $\tau = \tau_{11}$ confirm this PT prediction. Hence, Figs. 8(c) and 8(d) do not show any result for $\xi_1 = -\xi_2 = 0$.

For a pair of elliptically polarized pulses and a time delay τ_n with odd integer n, the change in the angular distribution predicted by the PT formulas (50) and (12) is in general complicated. However, for the special case that the relative CEP $\phi_{12} = 0$, Eqs. (50) and (12) predict the same $\pi/2$ shift of the angular distribution as in the case of circularly polarized pulses, but with a diminution of the amplitude owing to its dependence on the degree of linear polarization ℓ; i.e., the terms in square brackets in Eq. (50) reduce to $2(1-\ell)\sin^2\varphi$. These PT predictions in Fig. 8(d) are confirmed by our TDSE results in Fig. 8(c).

Finally, we note that the agreement of our TDSE results in Figs. 8(a) and 8(c) with our numerical PT results in Figs. 8(b) and 8(d) confirms our assumption that the He ground state depletion by the first of our two pulses is negligible.

VII. SUMMARY AND CONCLUSIONS

In summary, by means of both analytic PT analyses and direct numerical solution of the two-electron TDSE in six spatial dimensions for DPI of the He atom by a pair of time-delayed elliptically polarized attosecond pulses, we have analyzed the momentum and angular distributions of the ionized pair of electrons. In particular, our study has identified the conditions under which the two-electron momentum distributions exhibit spiral vortex patterns, which result from an unusual kind of Ramsey interference between the ionized electron wave packets produced by each attosecond pulse. Specifically, our analytic PT analysis has shown that *two-start* spiral vortex structures appear in the two-electron momentum distribution (i.e., the SDP) for any energy partitioning of the pair of electrons. However, they only occur in detection geometries for which the electron-electron correlation is “frozen” [53], i.e., for which the angular separation $\hat{\mathbf{p}}_1 \cdot \hat{\mathbf{p}}_2$ is held constant when detecting one of either the electron momenta $\mathbf{p}_{1,2}$ or the Jacobi momenta $\mathbf{P}_{\pm}$. These two-electron phenomena are exemplified numerically for several in-plane and out-of-plane detection geometries that satisfy the necessary conditions. These vortex features can also be seen in the FDP, i.e., the SDP averaged over the emission angles of one electron. However, in this case one must combine measurements of the FDP for two different detection geometries in order to subtract a spherically symmetric contribution that obscures the spiral vortex pattern in the polarization plane. As our results indicate, experimental observation of vortex-shaped momentum distributions (distorted or not), clockwise or counterclockwise, tightly wound or not, together with determination of the number of spiral arms and their energy width, represent signatures not only of the DPI process but also of the key parameters of the time-delayed counterrotating elliptically polarized attosecond pulses.

In addition, we have identified conditions under which one can control the angular distributions of the electrons. Specifically, for any energy-sharing scheme, the direction of the two photoelectrons can be controlled following single-photon DPI by the two oppositely elliptically polarized pulses by adjusting the time delay between the two pulses. Importantly, this fact implies exquisite control of electronic motion on an attosecond time scale.

Experimental observation of spiral vortex patterns in two-electron momentum distributions produced in DPI by a pair of time-delayed oppositely elliptically polarized attosecond pulses requires the ability to produce attosecond pulses with full control of the time delay between two pulses, their relative CEP, their polarizations, and their bandwidths. As DPI of He is a *linear* process, it does not require intense attosecond pulses. Reaction microscope techniques [67] already exist for measuring DPI momentum distributions. Isolated linearly polarized attosecond pulses with sufficient intensity also exist [10–12]. The production and control of elliptically polarized attosecond pulses is an active area of research [15–35]. The exquisite sensitivity of the vortex patterns in electron momentum distributions to the parameters of a pair of attosecond pulses makes them an ideal diagnostic tool for characterizing the attosecond pulses, which is a necessary requirement for their realization.

ACKNOWLEDGMENTS

The research of A.F.S. and J.M.N.D. is supported in part by the US Department of Energy (DOE), Office of Science, Basic Energy Sciences (BES), under Award No. DE-FG02-96ER14646; the research of S.X.H. is supported by the DOE National Nuclear Security Administration under Award No. DE-NA0001944, the University of Rochester, and the New York State Energy Research and Development Authority; the research of L.B.M. is supported by the VKR Center of Excellence, QUSCOPE; the research of A.V.M. is supported by the Russian Ministry of Education and Science under Grant No. 3.1761.2017/4.6. Computations were carried out using the Crane computing facilities of the Holland Computing Center at the University of Nebraska-Lincoln, as well as the Stampede (TACC) supercomputer under US National Science Foundation Grant No. PHY-120003.

APPENDIX A: CONVERGENCE TESTS FOR DPI BY TIME-DELAYED CIRCULARLY POLARIZED PULSES

All of the TDSE numerical results presented in this paper were tested for convergence. In this appendix, we illustrate results of these convergence tests for the specific case of the DPI angular distribution for the in-plane BTB detection geometry [Fig. 1(b)] at a *fixed* excess energy $E = \omega - E_g = 11$ eV and fixed energy sharing (with $\varepsilon = E_1/E = 17.5\%$) produced by a pair of right-left circularly polarized attosecond pulses delayed in time by $\tau = 275$ as. Specifically, we seek to find the time T_p after the end of the two pulses at which the angular distribution (1) converges. We have found that T_p does not depend on the helicity of the pair of pulses.

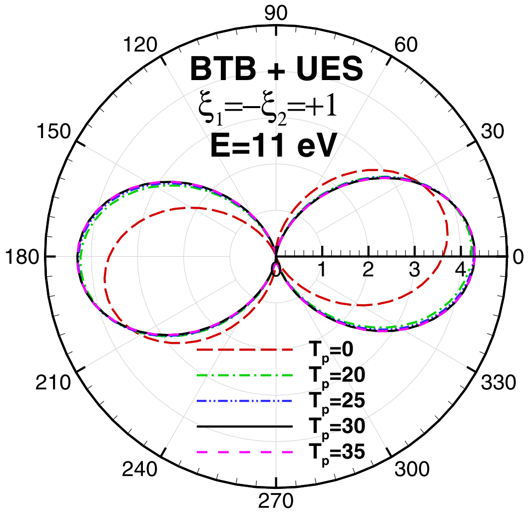

FIG. 9. Convergence of the DPI angular distribution [calculated using Eq. (1)] (in units of 10^{-7} a.u.) for the in-plane BTB detection geometry [Fig. 1(b)] at a *fixed* excess energy $E = \omega - E_g \simeq 11$ eV and fixed energy sharing $\varepsilon = E_1/E = 17.5\%$ produced by a pair of right-left circularly polarized xuv pulses delayed in time by $\tau = 275$ as. Results are shown at five times T_p after the end of the two pulses: 0, 20, 25, 30, and 35 a.u. The other pulse parameters are as in the caption of Fig. 2.

In Fig. 9 we show the results for the two-electron angular distributions obtained by projecting the double-continuum part of the TDSE two-electron final-state wave packet onto antisymmetrized Coulomb wave functions [see Eq. (1)] for five values of T_p. These results indicate that calculating this projection immediately after the end of the two pulses (i.e., at $T_p = 0$) is inaccurate since the doubly ionized wave packet has not yet entered the asymptotic region. As the observation time T_p increases, the two-electron angular distribution for the UES case shown in Fig. 9 converges for projection times T_p longer than 20 a.u. In contrast, the convergence of the two-electron angular distributions (not shown) for EES in the orthogonal out-of-plane detection geometry [Fig. 1(c)] only converge for projection times T_p longer than 40 a.u. Indeed, it is well established numerically [43] that the BTB UES configuration guarantees a high accuracy of our numerical method in the xuv regime (with convergence of our results for a relatively low number of individual electron angular momenta), as may be expected theoretically since the torque along the BTB axis is always zero [68] (see also [14]). In contrast, for EES cases the number of individual electron angular momenta increases logarithmically with time [68] (see also [14]).

APPENDIX B: THE SIXFOLD DIFFERENTIAL PROBABILITY AVERAGED OVER THE EMISSION ANGLES OF ONE ELECTRON

The SDP (2) averaged over the emission direction, $\hat{\mathbf{p}}_2$, of the electron momentum $\mathbf{p}_2$ is

$$\mathcal{W}(\mathbf{p}_1,p_2) \equiv \frac{d^4\mathcal{W}}{d\mathbf{p}_1 dp_2} = \int |A_1|^2 d\Omega_2, \tag{B1}$$

where A_1 is defined in Eq. (18) in terms of dynamical parameters $f_{1,2}(p_1,p_2,\cos\beta)$, and $d\Omega_2 = \sin\theta_2 d\theta_2 d\varphi_2$. Equation (B1) thus defines the FDP. Its evaluation in the $\mathbf{p}_{1,2}$ basis requires the following auxiliary relations:

$$\begin{aligned}\int \mathcal{F}(\cos\beta)(\mathbf{a}\cdot\hat{\mathbf{p}}_2)(\mathbf{b}\cdot\hat{\mathbf{p}}_2)d\Omega_2 =& \pi(\mathbf{a}\cdot\mathbf{b})\mathcal{F}_1\\ &+ \pi(\mathbf{a}\cdot\hat{\mathbf{p}}_1)(\mathbf{b}\cdot\hat{\mathbf{p}}_1)\mathcal{F}_2,\end{aligned} \tag{B2}$$

$$\int \mathcal{F}(\cos\beta)(\mathbf{a}\cdot\hat{\mathbf{p}}_2)\, d\Omega_2 = 2\pi\,(\mathbf{a}\cdot\hat{\mathbf{p}}_1)\mathcal{F}_3, \tag{B3}$$

where $\mathbf{a}$, $\mathbf{b}$ are arbitrary vectors, $\mathcal{F}$ is a function of the angle β between the photoelectron momenta, and the parameters $\mathcal{F}_i$ are defined by

$$\mathcal{F}_1 \equiv \int_{-1}^{1} \mathcal{F}(x)(1-x^2)dx,$$
$$\mathcal{F}_2 \equiv \int_{-1}^{1} \mathcal{F}(x)(3x^2-1)dx,$$
$$\mathcal{F}_3 \equiv \int_{-1}^{1} \mathcal{F}(x)x dx.$$

These equations can be proved by calculating the integrals in the coordinate frame whose z axis is directed along the vector $\mathbf{p}_1$. Using the relations (B2) and (B3), the FDP in Eq. (B1) takes the factorized form

$$\mathcal{W}(\mathbf{p}_1,p_2) = g_1(p_1,p_2)|\mathbf{e}'\cdot\hat{\mathbf{p}}_1|^2 + g_2(p_1,p_2)(\mathbf{e}'\cdot\mathbf{e}'^*), \tag{B4}$$

where the dynamical parameters $g_1(p_1,p_2) \equiv g_1$ and $g_2(p_1,p_2) \equiv g_2$ are related to the parameters $f_{1,2}$ by

$$g_1 = \pi J^2 \int_{-1}^{1} \{2x|f_1+f_2|^2 + (x-1)(3x+1)|f_2|^2\}dx, \tag{B5}$$

$$g_2 = \pi J^2 \int_{-1}^{1} (1-x^2)|f_2|^2 dx, \tag{B6}$$

where $x = \cos\beta$. Using Eq. (26) for the effective polarization vector $\mathbf{e}'$, Eq. (B4) can be rewritten as

$$\begin{aligned}\mathcal{W}(\mathbf{p}_1,p_2) =& g_1(p_1,p_2)[|\mathbf{e}_1\cdot\hat{\mathbf{p}}_1|^2 + |\mathbf{e}_2\cdot\hat{\mathbf{p}}_1|^2\\ &+ 2\,\mathrm{Re}\{(\mathbf{e}_1\cdot\hat{\mathbf{p}}_1)(\mathbf{e}_2{}^*\cdot\hat{\mathbf{p}}_1)\exp(-i\Phi)\}]\\ &+ 2g_2(p_1,p_2)[1 + \mathrm{Re}\{(\mathbf{e}_1\cdot\mathbf{e}_2^*)\exp(-i\Phi)\}].\end{aligned} \tag{B7}$$

In special cases, Eq. (B7) simplifies considerably, as discussed below.

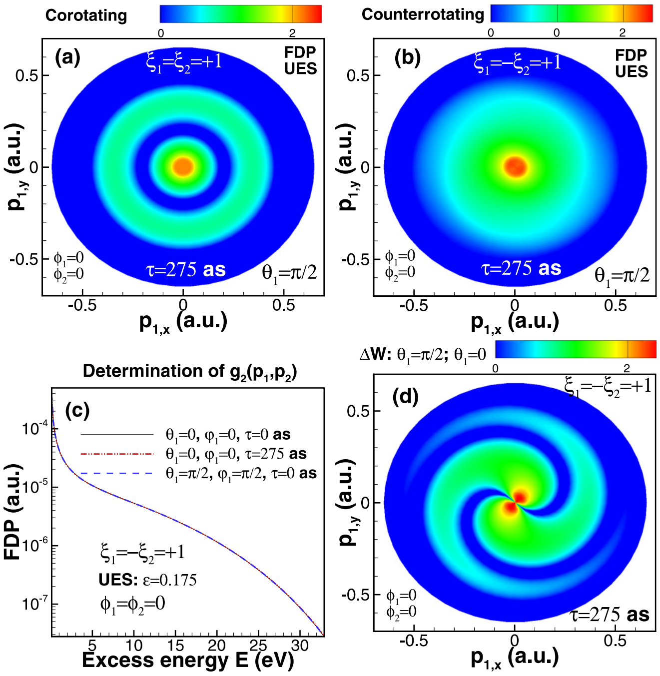

FIG. 10. Fourfold differential probability (FDP) [i.e., the SDP (1) averaged over the emission angles, $\hat{\mathbf{p}}_2$], $\mathcal{W}(\mathbf{p}_1;p_2)$, in the polarization plane ($\theta_1 = \pi/2$) by a pair of time-delayed ($\tau = 275$ as) attosecond pulses that are (a) right-right or (b) right-left circularly polarized. (c) Three independent calculations of the FDP for parameters that allow one to directly determine the energy dependence of $g_2(p_1,p_2)$ in Eq. (B6) (see figure legends and text discussion). (d) TDSE results for $\Delta\mathcal{W} = |\mathcal{W}(p_1,\theta_1,\varphi_1;p_2) - \mathcal{W}(p_1,\theta_1',\varphi_1;p_2)|$ in Eq. (B10) obtained by subtracting FDP results for two detection geometries: $\theta_1 = \pi/2$ and $\theta_1' = 0$. The color scale shows the FDPs in units of 10^{-4} a.u. [(a), (b)] and 10^{-5} a.u. (d). The pulse parameters are as in the caption of Fig. 2.

Consider first the case of two identically polarized pulses, i.e., $\mathbf{e}_1 = \mathbf{e}_2$, for which Eq. (B7) becomes

$$\mathcal{W}(\mathbf{p}_1,p_2) = 4\cos^2(\Phi/2)(g_1|\mathbf{e}_1\cdot\hat{\mathbf{p}}_1|^2 + g_2), \tag{B8}$$

where the parameters $g_{1,2}$ [defined by Eqs. (B5) and (B6) in terms of $f_{1,2}$] are functions of p_1,p_2 only. One sees that the magnitude of the FDP in Eq. (B8) is proportional to the Ramsey interference factor $\cos^2(\Phi/2)$. Owing to the spherical symmetry of $g_{1,2}(p_1,p_2)$, when the time-delayed pulses are circularly polarized, the in-plane momentum distributions exhibit Newton's rings [44]. This PT prediction is confirmed by our TDSE results for the FDP in Fig. 10(a), which shows the $\mathbf{p}_1$ distribution for UES (with $\varepsilon = E_1/E = 17.5\%$) produced by right-right circularly polarized pulses delayed in time by $\tau = 275$ as.

For oppositely circularly polarized pulses, $\mathbf{e}_1 = \mathbf{e}_2^* = \mathbf{e}$ and $\xi \equiv \xi_1 = -\xi_2 = \pm 1$. Using the geometric factor (29), the FDP (B7) becomes

$$\mathcal{W}(\mathbf{p}_1,p_2) = 2[g_1\sin^2\theta_1\cos^2(\varphi_1 - \xi\Phi/2) + g_2]. \tag{B9}$$

The structure of this FDP is similar to that for the case of single-electron photoionization by a pair of time-delayed, oppositely circularly polarized attosecond pulses [44], except for the presence of the spherically symmetric term $g_2(p_1,p_2)$. If the magnitude of $g_2(p_1,p_2)$ is comparable to or greater than $g_1(p_1,p_2)$, measurement of the FDP in the polarization plane may not exhibit the spiral vortex patterns generated by the first term in Eq. (B9). In such cases, in order to observe the spiral vortex patterns in the polarization plane ($\theta_1 = \pi/2$) described by the factor $\cos^2(\varphi_1 - \xi\Phi/2)$ in the first term of the FDP in Eq. (B9), we must determine the function $2g_2(p_1,p_2)$ and subtract it from Eq. (B9). In other words, we must make measurements of the momentum distributions (B9) for *two different polar angles*, θ_1 and θ_1'. Subtracting the results of these two measurements, i.e., $\Delta\mathcal{W} \equiv |\mathcal{W}(p_1,\theta_1,\varphi_1;\, p_2) - \mathcal{W}(p_1,\theta_1',\varphi_1;\, p_2)|$, we obtain from Eq. (B9) the result

$$\Delta\mathcal{W} = 2|(\sin^2\theta_1 - \sin^2\theta_1')g_1|\cos^2(\varphi_1 - \xi\Phi/2). \qquad \text{(B10)}$$

Since g_1 depends on p_1,p_2 only, the magnitude of $\Delta\mathcal{W}$ has maxima at $\varphi_1 = \xi\Phi/2 + \pi n$ and minima at $\varphi_1 = \xi\Phi/2 + \pi(n + 1/2)$, with n an arbitrary integer. These conditions define Fermat spirals in the plane with polar coordinates p_1,φ_1.

We illustrate in Figs. 10(b)–10(d) this two-measurement procedure for observing the spiral vortices in the FDP. Our numerically calculated $\mathbf{p}_1$ distribution (FDP) for an UES configuration with $\varepsilon = E_1/E = 17.5\%$ by right-left circularly polarized attosecond pulses delayed in time by $\tau = 275$ as, with each pulse having a zero CEP, is shown in Fig. 10(b). The shape of the $\mathbf{p}_1$ distribution in Fig. 10(b) is consistent with PT formula (B9), as the occurrence of the vortex structure is obscured by the isotropic $g_2(p_1,p_2)$ term. In Fig. 10(c) we show numerical TDSE results for the FDP for three cases in which the first term in brackets in the PT Eq. (B9) vanishes: (i) $\theta_1 = 0$, $\phi_1 = 0$, and $\tau = 0$, (ii) $\theta_1 = 0$, $\phi_1 = 0$, and $\tau = 275$ as, and (iii) $\theta_1 = \pi/2$, $\phi_1 = \pi/2$, and $\tau = 0$. As shown in Fig. 10(c), our TDSE numerical results for the FDP in Eq. (B9) for each of these three cases gives the same energy dependence for $2g_2(p_1,p_2)$. As predicted by PT formula (B10), our TDSE results in Fig. 10(d) show that *two-arm* spiral vortex patterns occur in the $\mathbf{p}_1$ distribution for $\Delta\mathcal{W}$, which is obtained by subtracting the FDP for detecting $\mathbf{p}_1$ along $\hat{\mathbf{k}}$ (i.e., $\theta_1' = 0$) from the FDP for detecting $\mathbf{p}_1$ in the polarization plane (i.e., $\theta_1 = \pi/2$).

---

[1] F. W. Byron and C. J. Joachain, Multiple ionization processes in helium, Phys. Rev. **164**, 1 (1967).

[2] D. Proulx and R. Shakeshaft, Double ionization of helium by a single photon with energy 89–140 eV, Phys. Rev. A **48**, R875(R) (1993).

[3] P. Lablanquie, J. Mazeau, L. Andric, P. Selles, and A. Huetz, Effect of Electron Energy Sharing on the Double Photoionization of Helium near Threshold, Phys. Rev. Lett. **74**, 2192 (1995).

[4] R. Dörner, J. M. Feagin, C. L. Cocke, H. Bräuning, O. Jagutzki, M. Jung, E. P. Kanter, H. Khemliche, S. Kravis, V. Mergel, M. H. Prior, H. Schmidt-Böcking, L. Spielberger, J. Ullrich, M. Unversagt, and T. Vogt, Fully Differential Cross Sections for Double Photoionization of He Measured by Recoil Ion Momentum Spectroscopy, Phys. Rev. Lett. **77**, 1024 (1996).

[5] H. Braüning, R. Dörner, C. L. Cocke, M. H. Prior, B. Krässig, A. S. Kheifets, I. Bray, A. Bräuning-Demian, K. Carnes, S. Dreuil, V. Mergel, R. Richard, J. Ullrich and H. Schmidt-Böcking, Absolute triple differential cross sections for photo-double ionization of helium—experiment and theory, J. Phys. B **31**, 5149 (1998).

[6] J. S. Briggs and V. Schmidt, Differential cross sections for photo-double-ionization of the helium atom, J. Phys. B **33**, R1 (2000).

[7] L. Malegat, P. Selles, and A. K. Kazansky, Absolute Differential Cross Sections for Photo Double Ionization of Helium from the *Ab Initio* Hyperspherical *R*-Matrix Method with Semiclassical Outgoing Waves, Phys. Rev. Lett. **85**, 4450 (2000).

[8] P. M. Paul, E. S. Toma, P. Breger, G. Mullot, F. Augé, P. Balcou, H. G. Muller, and P. Agostini, Observation of a train of attosecond pulses from high harmonic generation, Science **292**, 1689 (2001).

[9] M. Hentschel, R. Kienberger, C. Spielmann, G. A. Reider, N. Milosevic, T. Brabec, P. Corkum, U. Heinzmann, M. Drescher, and F. Krausz, Attosecond metrology, Nature (London) **414**, 509 (2001).

[10] G. Sansone, E. Benedetti, F. Calegari, C. Vozzi, L. Avaldi, R. Flammini, L. Poletto, P. Villoresi, C. Altucci, R. Velotta, S. Stagira, S. D. Silvestri, and M. Nisoli, Isolated single-cycle attosecond pulses, Science **314**, 443 (2006).

[11] E. Goulielmakis, M. Schultze, M. Hofstetter, V. S. Yakovlev, J. Gagnon, M. Uiberacker, A. L. Aquila, E. M. Gullikson, D. T. Attwood, R. Kienberger, F. Krausz, and U. Kleineberg, Single-cycle nonlinear optics, Science **320**, 1614 (2008).

[12] K. Zhao, Q. Zhang, M. Chini, Y. Wu, X. Wang, and Z. Chang, Tailoring a 67 attosecond pulse through advantageous phase-mismatch, Opt. Lett. **37**, 3891 (2012).

[13] E. Foumouo, P. Antoine, H. Bachau, and B. Piraux, Attosecond timescale analysis of the dynamics of two-photon double ionization of helium, New J. Phys. **10**, 025017 (2008).

[14] E. Foumouo, A. Hamido, P. Antoine, B. Piraux, H. Bachau, and R. Shakeshaft, Time-dependent analysis of the mechanism for two-photon double escape in helium: From very long to attosecond time scales, J. Phys. B **43**, 091001 (2010).

[15] H. Eichmann, A. Egbert, S. Nolte, C. Momma, B. Wellegehausen, W. Becker, S. Long, and J. K. McIver, Polarization-dependent high-order two-color mixing, Phys. Rev. A **51**, R3414(R) (1995).

[16] F. A. Weihe, S. K. Dutta, G. Korn, D. Du, P. H. Bucksbaum, and P. L. Shkolnikov, Polarization of high-intensity high-harmonic generation, Phys. Rev. A **51**, R3433(R) (1995).

[17] S. Long, W. Becker, and J. K. McIver, Model calculations of polarization-dependent two-color high-harmonic generation, Phys. Rev. A **52**, 2262 (1995).

[18] X.-M. Tong and S.-I. Chu, Generation of circularly polarized multiple high-order harmonic emission from two-color crossed laser beams, Phys. Rev. A **58**, R2656(R) (1998).

[19] W. Becker, B. N. Chichkov, and B. Wellegehausen, Schemes for the generation of circularly polarized high-order harmonics by two-color mixing, Phys. Rev. A **60**, 1721 (1999).

[20] D. B. Milošević, W. Becker, and R. Kopold, Generation of circularly polarized high-order harmonics by two-color coplanar field mixing, Phys. Rev. A **61**, 063403 (2000).

[21] D. B. Milošević and W. Becker, Attosecond pulse trains with unusual nonlinear polarization, Phys. Rev. A **62**, 011403(R) (2000).

[22] B. Vodungbo, A. B. Sardinha, J. Gautier, G. Lambert, C. Valentin, M. Lozano, G. Iaquaniello, F. Delmotte, S. Sebban, J. Lüning, and P. Zeitoun, Polarization control of high order harmonics in the EUV photon energy range, Opt. Express **19**, 4346 (2011).

[23] K.-J. Yuan and A. D. Bandrauk, Generation of circularly polarized attosecond pulses by intense ultrashort laser pulses from extended asymmetric molecular ions, Phys. Rev. A **84**, 023410 (2011).

[24] K.-J. Yuan and A. D. Bandrauk, Circularly polarized attosecond pulses from molecular high-order harmonic generation by ultrashort intense bichromatic circularly and linearly polarized laser pulses, J. Phys. B **45**, 074001 (2012).

[25] F. Morales, I. Barth, V. Serbinenko, S. Patchkovskii, and O. Smirnova, Shaping polarization of attosecond pulses via laser control of electron and hole dynamics, J. Mod. Opt. **59**, 1303 (2012).

[26] K.-J. Yuan and A. D. Bandrauk, Single Circularly Polarized Attosecond Pulse Generation by Intense Few Cycle Elliptically Polarized Laser Pulses and Terahertz Fields from Molecular Media, Phys. Rev. Lett. **110**, 023003 (2013).

[27] M. Ivanov and E. Pisanty, Taking control of polarization, Nat. Photonics **8**, 501 (2014).

[28] A. Fleischer, O. Kfir, T. Diskin, P. Sidorenko, and O. Cohen, Spin angular momentum and tunable polarization in high-harmonic generation, Nat. Photonics **8**, 543 (2014).

[29] E. Pisanty, S. Sukiasyan, and M. Ivanov, Spin conservation in high-order-harmonic generation using bicircular fields, Phys. Rev. A **90**, 043829 (2014).

[30] A. Ferré, C. Handschin, M. Dumergue, F. Burgy, A. Comby, D. Descamps, B. Fabre, G. A. Garcia, R. Géneaux, L. Merceron, E. Mével, L. Nahon, S. Petit, B. Pons, D. Staedter, S. Weber, T. Ruchon, V. Blanchet, and Y. Mairesse, A table-top ultrashort light source in the extreme ultraviolet for circular dichroism experiments, Nat. Photonics **9**, 93 (2015).

[31] O. Kfir, P. Grychtol, E. Turgut, R. Knut, D. Zusin, D. Popmintchev, T. Popmintchev, H. Nembach, J. M. Shaw, A. Fleischer, H. Kapteyn, M. Murnane, and O. Cohen, Generation of bright phase-matched circularly polarized extreme ultraviolet high harmonics, Nat. Photonics **9**, 99 (2015).

[32] F. Chen, J. Luo, and F. Luo, Single circularly polarized attosecond pulse generation by spatially inhomogeneous fields from atoms with nonvanishing angular quantum number, Opt. Commun. **342**, 68 (2015).

[33] G. Lambert, B. Vodungbo, J. Gautier, B. Mahieu, V. Malka, S. Sebban, P. Zeitoun, J. Luning, J. Perron, A. Andreev, S. Stremoukhov, F. Ardana-Lamas, A. Dax, C. P. Hauri, A. Sardinha, and M. Fajardo, Towards enabling femtosecond helicity-dependent spectroscopy with high-harmonic sources, Nat. Commun. **6**, 6167 (2015).

[34] L. Medišauskas, J. Wragg, H. v. d. Hart, and M. Y. Ivanov, Generating Isolated Elliptically Polarized Attosecond Pulses using Bichromatic Counterrotating Circularly Polarized Laser Fields, Phys. Rev. Lett. **115**, 153001 (2015).

[35] C. Hernández-García, C. G. Durfee, D. D. Hickstein, T. Popmintchev, A. Meier, M. M. Murnane, H. C. Kapteyn, I. J. Sola, A. Jaron-Becker, and A. Becker, Schemes for generation of isolated attosecond pulses of pure circular polarization, Phys. Rev. A **93**, 043855 (2016).

[36] I. Powis, Photoelectron circular dichroism of the randomly oriented chiral molecules glyceraldehyde and lactic acid, J. Chem. Phys. **112**, 301 (2000).

[37] N. Böwering, T. Lischke, B. Schmidtke, N. Müller, T. Khalil, and U. Heinzmann, Asymmetry in Photoelectron Emission from Chiral Molecules Induced by Circularly Polarized Light, Phys. Rev. Lett. **86**, 1187 (2001).

[38] U. Hergenhahn, E. E. Rennie, O. Kugeler, S. Marburger, T. Lischke, I. Powis, and G. Garcia, Photoelectron circular dichroism in core level ionization of randomly oriented pure enantiomers of the chiral molecule camphor, J. Chem. Phys. **120**, 4553 (2004).

[39] S. Eisebitt, J. Lüning, W. F. Schlotter, M. Lörgen, O. Hellwig, W. Eberhardt, and J. Stöhr, Lensless imaging of magnetic nanostructures by x-ray spectro-holography, Nature (London) **432**, 885 (2004).

[40] C. Boeglin, E. Beaurepaire, V. Halté, V. López-Flores, C. Stamm, N. Pontius, H. A. Dürr, and J.-Y. Bigot, Distinguishing the ultrafast dynamics of spin and orbital moments in solids, Nature (London) **465**, 458 (2010).

[41] I. Radu, K. Vahaplar, C. Stamm, T. Kachel, N. Pontius, H. A. Dürr, T. A. Ostler, J. Barker, R. F. L. Evans, R. W. Chantrell, A. Tsukamoto, A. Itoh, A. Kirilyuk, T. Rasing, and A. V. Kimel, Transient ferromagnetic-like state mediating ultrafast reversal of antiferromagnetically coupled spins, Nature (London) **472**, 205 (2011).

[42] V. López-Flores, J. Arabski, C. Stamm, V. Halté, N. Pontius, E. Beaurepaire, and C. Boeglin, Time-resolved x-ray magnetic circular dichroism study of ultrafast demagnetization in a CoPd ferromagnetic film excited by circularly polarized laser pulse, Phys. Rev. B **86**, 014424 (2012).

[43] J. M. N. Djiokap, N. L. Manakov, A. V. Meremianin, S. X. Hu, L. B. Madsen, and A. F. Starace, Nonlinear Dichroism in Back-to-Back Double Ionization of He by An Intense Elliptically Polarized Few-Cycle Extreme Ultraviolet Pulse, Phys. Rev. Lett. **113**, 223002 (2014).

[44] J. M. N. Djiokap, S. X. Hu, L. B. Madsen, N. L. Manakov, A. V. Meremianin, and A. F. Starace, Electron Vortices in Photoionization by Circularly Polarized Attosecond Pulses, Phys. Rev. Lett. **115**, 113004 (2015).

[45] J. M. N. Djiokap, A. V. Meremianin, N. L. Manakov, S. X. Hu, L. B. Madsen, and A. F. Starace, Multistart spiral electron vortices in ionization by circularly polarized pulses, Phys. Rev. A **94**, 013408 (2016).

[46] M. Harris, C. A. Hill, and J. M. Vaughan, Optical helices and spiral interference fringes, Opt. Commun. **106**, 161 (1994).

[47] K.-J. Yuan, S. Chelkowski, and A. D. Bandrauk, Photoelectron momentum distributions of molecules in bichromatic circularly polarized attosecond uv laser fields, Phys. Rev. A **93**, 053425 (2016).

[48] D. Pengel, S. Kerbstadt, D. Johannmeyer, L. Englert, T. Bayer, and M. Wollenhaupt, Electron Vortices in Femtosecond Multiphoton Ionization, Phys. Rev. Lett. **118**, 053003 (2017).

[49] C. A. Mancuso, D. D. Hickstein, P. Grychtol, R. Knut, O. Kfir, X.-M. Tong, F. Dollar, D. Zusin, M. Gopalakrishnan, C. Gentry, E. Turgut, J. L. Ellis, M.-C. Chen, A. Fleischer, O. Cohen, H. C. Kapteyn, and M. M. Murnane, Strong-field ionization with two-color circularly polarized laser fields, Phys. Rev. A **91**, 031402(R) (2015).

[50] N. Douguet, A. N. Grum-Grzhimailo, E. V. Gryzlova, E. I. Staroselskaya, J. Venzke, and K. Bartschat, Photoelectron angular distributions in bichromatic atomic ionization induced by circularly polarized vuv femtosecond pulses, Phys. Rev. A **93**, 033402 (2016).

[51] J. M. Feagin, Recoil-ion angular distributions following double photoionization, J. Phys. B **29**, L551 (1996).

[52] M. Walter, A. V. Meremianin, and J. S. Briggs, Multi-particle photoionization by a single photon, J. Phys. B **36**, 4561 (2003).

[53] M. Gisselbrecht, M. Lavollée, A. Huetz, P. Bolognesi, L. Avaldi, D. P. Seccombe, and T. J. Reddish, Photodouble Ionization Dynamics for Fixed-in-Space H_2, Phys. Rev. Lett. **96**, 153002 (2006).

[54] M. S. Pindzola and F. Robicheaux, Total ionization cross section for electron-hydrogen scattering using a time-dependent close-coupling method, Phys. Rev. A **54**, 2142 (1996).

[55] M. S. Pindzola and F. Robicheaux, Time-dependent close-coupling calculations of correlated photoionization processes in helium, Phys. Rev. A **57**, 318 (1998).

[56] C. W. McCurdy, M. Baertschy, and T. N. Rescigno, Solving the three-body Coulomb breakup problem using exterior complex scaling, J. Phys. B **37**, R137 (2004).

[57] S. X. Hu, Optimizing the FEDVR-TDCC code for exploring the quantum dynamics of two-electron systems in intense laser pulses, Phys. Rev. E **81**, 056705 (2010).

[58] J. M. N. Djiokap, S. X. Hu, W.-C. Jiang, L.-Y. Peng, and A. F. Starace, Enhanced asymmetry in few-cycle attosecond pulse ionization of He in the vicinity of autoionizing resonances, New J. Phys. **14**, 095010 (2012).

[59] J. M. N. Djiokap, S. X. Hu, W.-C. Jiang, L.-Y. Peng, and A. F. Starace, Asymmetries in production of $\mathrm{He}^+(n = 2)$ with an intense few-cycle attosecond pulse, Phys. Rev. A **88**, 011401(R) (2013).

[60] J. M. N. Djiokap, N. L. Manakov, A. V. Meremianin, and A. F. Starace, Carrier-envelope-phase-induced asymmetries in double ionization of helium by an intense few-cycle xuv pulse, Phys. Rev. A **88**, 053411 (2013).

[61] H. G. Muller, An efficient propagation scheme for the time-dependent Schrödinger equation in the velocity gauge, Laser Phys. **9**, 138 (1999).

[62] T. K. Kjeldsen, L. A. A. Nikolopoulos, and L. B. Madsen, Solving the m-mixing problem for the three-dimensional time-dependent Schrödinger equation by rotations: Application to strong-field ionization of H_2^+, Phys. Rev. A **75**, 063427 (2007).

[63] L. B. Madsen, L. A. A. Nikolopoulos, T. K. Kjeldsen, and J. Fernández, Extracting continuum information from $\Psi(t)$ in time-dependent wave-packet calculations, Phys. Rev. A **76**, 063407 (2007).

[64] A. Y. Istomin, N. L. Manakov, A. V. Meremianin, and A. F. Starace, Nondipole Effects in Photo-Double-Ionization of He by a vuv Photon, Phys. Rev. Lett. **92**, 063002 (2004).

[65] C. P. J. Martiny and L. B. Madsen, Symmetry of Carrier-Envelope Phase Difference Effects in Strong-Field, Few-Cycle Ionization of Atoms and Molecules, Phys. Rev. Lett. **97**, 093001 (2006).

[66] See Supplemental Material at http://link.aps.org/supplemental/10.1103/PhysRevA.96.013405 for animations of the evolution of vortex patterns with time delay τ over the range $0 \leqslant \tau \leqslant 550$ as for the BTB UES geometry and the same laser parameters as in Fig. 5(e) for the two cases of right-left and left-right circularly polarized attosecond pulses (i.e., $\xi_1 = -\xi_2 = \pm 1$).

[67] J. Ullrich, R. Moshammer, A. Dorn, R. Dörner, L. P. H. Schmidt, and H. Schmidt-Böcking, Recoil-ion and electron momentum spectroscopy: Reaction-microscopes, Rep. Prog. Phys. **66**, 1463 (2003).

[68] M. Gailitis, The behavior of particles' angular momenta in scattering processes with three or more charged particles, J. Phys. B **23**, 85 (1990).